Seismic interferometry by crosscorrelation and by multi-dimensional deconvolution: a systematic comparison

Kees Wapenaar, Joost van der Neut, Elmer Ruigrok, Deyan Draganov, Jürg Hunziker, Evert Slob, Jan Thorbecke,
Department of Geotechnology, Delft University of Technology, P.O. Box 5048, 2600 GA Delft, The Netherlands,

Roel Snieder
Center for Wave Phenomena, Colorado School of Mines, Golden, Colorado 80401, USA.

1 January 2011

SUMMARY

Seismic interferometry, also known as Green's function retrieval by crosscorrelation, has a wide range of applications, ranging from surface wave tomography using ambient noise, to creating virtual sources for improved reflection seismology. Despite its successful applications, the crosscorrelation approach also has its limitations. The main underlying assumptions are that the medium is lossless and that the wave field is equipartitioned. These assumptions are in practice often violated: the medium of interest is often illuminated from one side only, the sources may be irregularly distributed, and, particularly for EM applications, losses may be significant. These limitations may partly be overcome by reformulating seismic interferometry as a multidimensional deconvolution (MDD) process. We present a systematic analysis of seismic interferometry by crosscorrelation and by MDD. We show that for the non-ideal situations mentioned above, the correlation function is proportional to a Green's function with a blurred source. The source blurring is quantified by a so-called point-spread function which, like the correlation function, can be derived from the observed data (i.e., without the need to know the sources and the medium). The source of the Green's function obtained by the correlation method can be deblurred by deconvolving the correlation function for the point-spread function. This is the essence of seismic interferometry by MDD. We illustrate the crosscorrelation and MDD methods for controlled-source and passive data applications with numerical examples and discuss the advantages and limitations of both methods.

Key words: seismic interferometry, crosscorrelation, deconvolution, ambient noise, virtual source

1 INTRODUCTION

In recent years, the methodology of Green's function retrieval by crosscorrelation has led to many applications in seismology (exploration, regional and global), underwater acoustics and ultrasonics. In seismology this methodology is also called "seismic interferometry". One of the explanations for the broad interest lies in the fact that new responses can be obtained from measured data in a very simple way. In passive-data applications, a straightforward crosscorrelation of responses at two receivers gives the impulse response (Green's function) at one receiver of a virtual source at the position of the other. In controlled-source applications the procedure is similar, except that it involves in addition a summation over the sources. For a review of the theory and the many applications of seismic interferometry, see Larose et al. (2006), Schuster (2009) and Snieder et al. (2009). ~~and Wapenaar et al., (2010a,b).~~

It has also been recognized that the simple crosscorrelation approach has its limitations. From the various theoretical models it follows that there are a number of underlying assumptions for retrieving the Green's function by cross-correlation. The most important assumptions are that the medium is lossless and that the waves are equipartitioned. In heuristic terms, the latter condition means that the receivers are illuminated isotropically from all directions, which is for example achieved when the sources are regularly distributed along a closed surface, the sources are mutually uncorrelated and their power spectra are identical. Despite the fact that in practical situations these conditions are at most only partly fulfilled, the results of seismic interferometry are generally quite robust, but the retrieved amplitudes are unreliable and the results are often blurred by artifacts.

Several researchers have proposed to address some of the shortcomings by replacing the correlation process by deconvolution. In the "virtual source method" pioneered by Bakulin & Calvert (2004) the main limitation is that the real sources are present only at the Earth's surface, i.e., above the downhole receivers, instead of on a closed surface surrounding the receivers, as prescribed by the theory (Wapenaar et al. 2005; van Manen et al. 2005; Korneev & Bakulin 2006). To compensate for this one-sided illumination, Bakulin & Calvert (2006) propose to replace the cor-

relation by a deconvolution for the downgoing wave field at the downhole receivers. They show that this approach compensates for variations in the source wavelet and, partly, for reverberations in the overburden. Snieder et al. (2006a) deconvolve passive wave fields observed at different depth levels and show that, apart from compensating for the source function, this methodology also changes the boundary conditions of the system. ~~in an advantageous way~~. They applied it to earthquake data recorded at different heights in the Millikan library in Pasadena and obtained the impulse response of the building. Mehta et al. (2007b) used a similar approach to estimate the near-surface properties of the Earth from passive recordings in a vertical borehole. Vasconcelos & Snieder (2008a,b) and Vasconcelos et al. (2008) used deconvolution interferometry in seismic imaging with complicated and unknown source-time signals and for imaging with internal multiples. All these approaches improve seismic interferometry to some extent. An important positive aspect is that the required processing in all these cases is not much more complicated than in the correlation approach because the employed deconvolution procedures are essentially 1-D (i.e., trace-by-trace deconvolution). This compensates for variations in the source wavelet, anelastic losses and, partly, for internal multiples, but it does not account for the anisotropic illumination of the receivers.

To obtain more accurate results, seismic interferometry by deconvolution should acknowledge the 3-D nature of the seismic wave field. Hence, from a theoretical point of view, the trace-by-trace deconvolution process should be replaced by a full 3-D wave field deconvolution process. In the following we speak of multi-dimensional deconvolution (MDD), which stands for 3-D wave field deconvolution in the 3-D situation, or for 2-D wave field deconvolution in the 2-D situation. The MDD principle is not entirely new. It has been applied for example for multiple elimination of ocean-bottom data (Wapenaar et al. 2000; Amundsen 2001). Like the aforementioned method of Snieder et al. (2006a), this can be seen as a methodology that changes the boundary conditions of the system: it transforms the response of the subsurface including the effects of the reflecting ocean bottom and water surface into the response of a subsurface without these reflecting boundaries. With hindsight this methodology appears to be an extension of a 1-D deconvolution approach proposed by Riley & Claerbout (1976). Muijs et al. (2007) employ multi-dimensional deconvolution for the downgoing wave field (including multiples) in the imaging condition, thus improving the illumination and resolution of the imaged structures. Schuster & Zhou (2006) and Wapenaar et al. (2008a) discuss MDD of controlled-source data in the context of seismic interferometry. Slob et al. (2007) apply MDD to modeled controlled-source electromagnetic (CSEM) data and demonstrate the relative insensitivity to dissipation as well as the potential of changing the boundary conditions: the effect of the air wave, a notorious problem in CSEM prospecting, is largely suppressed. Wapenaar et al. (2008b) apply MDD to passive seismic data and show how it corrects for anisotropic illumination due to an irregular source distribution. van der Neut & Bakulin (2009) show how MDD can be used to improve the radiation pattern of a virtual source. In a related method called "directional balancing", Curtis & Halliday (2010) deconvolve the cross-
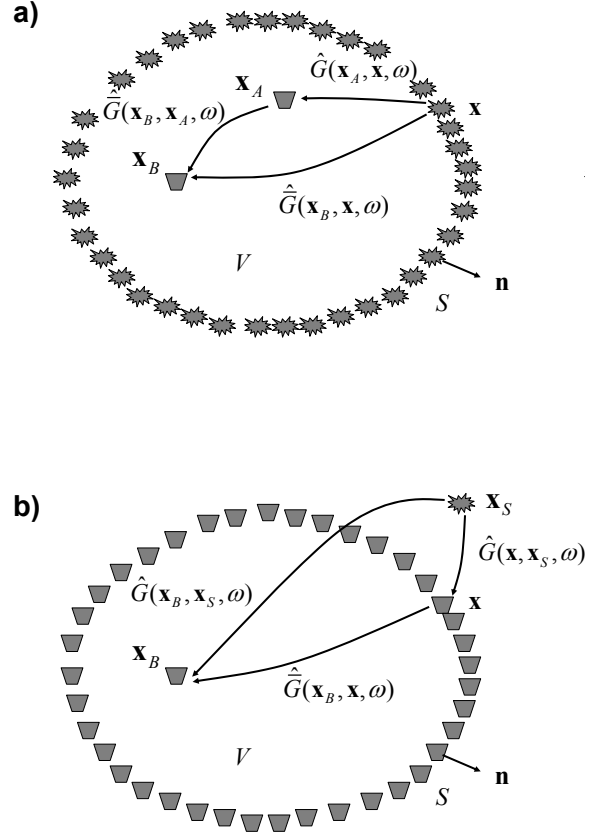

Figure 1. *(a) Configuration for the correlation-type Green's function representation (equation 1). The medium in $\mathbb{V}$ is assumed lossless. The rays represent full responses, including primary and multiple scattering due to inhomogeneities inside as well as outside $\mathbb{S}$. The notation $\hat{\bar{G}}$ refers to a reference state with possibly different boundary conditions at $\mathbb{S}$ and/or different medium parameters outside $\mathbb{S}$ (in $\mathbb{V}$ the medium parameters are the same for $\hat{G}$ and $\hat{\bar{G}}$). (b) Configuration for the convolution-type Green's function representation (equation 2). Here the medium does not need to be lossless.*

correlation result by the estimated radiation pattern of the virtual source.

Interferometry by MDD is more accurate than the trace-by-trace correlation and deconvolution approaches but the processing is more involved. In this paper we present a systematic analysis of seismic interferometry by crosscorrelation versus multi-dimensional deconvolution and discuss applications of both approaches.

2 GREEN'S FUNCTION REPRESENTATIONS FOR SEISMIC INTERFEROMETRY

We briefly review two Green's function representations for seismic interferometry. Consider a volume $\mathbb{V}$ enclosed by a surface $\mathbb{S}$, with outward pointing normal vector $\mathbf{n} = (n_1, n_2, n_3)$. In $\mathbb{V}$ we have an arbitrary inhomogeneous

medium with acoustic propagation velocity $c(\mathbf{x})$ and mass density $\rho(\mathbf{x})$ (where $\mathbf{x} = (x_1, x_2, x_3)$ is the Cartesian coordinate vector). We consider two points in $\mathbb{V}$, denoted by coordinate vectors $\mathbf{x}_A$ and $\mathbf{x}_B$, see Figure 1a. We define the Fourier transform of a time-dependent function $u(t)$ as $\hat{u}(\omega) = \int_{-\infty}^{\infty} \exp(-j\omega t) u(t) \mathrm{d}t$, with j the imaginary unit and ω the angular frequency. Assuming the medium in $\mathbb{V}$ is lossless, the correlation-type representation for the acoustic Green's function between $\mathbf{x}_A$ and $\mathbf{x}_B$ in $\mathbb{V}$ reads (Wapenaar et al. 2005; van Manen et al. 2005)

$$\hat{\bar{G}}(\mathbf{x}_B, \mathbf{x}_A, \omega) + \hat{G}^*(\mathbf{x}_B, \mathbf{x}_A, \omega) = \qquad (1)$$
$$-\oint_{\mathbb{S}} \frac{1}{j\omega\rho(\mathbf{x})} \Big(\partial_i \hat{\bar{G}}(\mathbf{x}_B, \mathbf{x}, \omega) \hat{G}^*(\mathbf{x}_A, \mathbf{x}, \omega)$$
$$-\hat{\bar{G}}(\mathbf{x}_B, \mathbf{x}, \omega) \partial_i \hat{G}^*(\mathbf{x}_A, \mathbf{x}, \omega) \Big) n_i \, \mathrm{d}\mathbf{x}$$

(Einstein's summation convention applies to repeated lower case Latin subscripts). This representation is the basic expression for seismic interferometry (or Green's function retrieval) by crosscorrelation in open systems. The superscript asterisk * denotes complex conjugation, hence, the products on the right-hand side correspond to crosscorrelations in the time domain of observations at two receivers at $\mathbf{x}_A$ and $\mathbf{x}_B$. The notation $\hat{\bar{G}}$ is introduced to denote a reference state with possibly different boundary conditions at $\mathbb{S}$ and/or different medium parameters outside $\mathbb{S}$ (but in $\mathbb{V}$ the medium parameters for $\hat{\bar{G}}$ are the same as those for $\hat{G}$). The bar is usually omitted because $\hat{G}$ and $\hat{\bar{G}}$ are usually defined in the same medium throughout space. The Green's functions on the left-hand side are the Fourier transforms of the response of a source at $\mathbf{x}_A$ observed at $\mathbf{x}_B$ and its time-reversed version. Representation (1) is exact, hence, it accounts not only for the direct wave, but also for primary and multiply scattered waves. Note that the inverse Fourier transform of the left-hand side gives $\bar{G}(\mathbf{x}_B, \mathbf{x}_A, t) + G(\mathbf{x}_B, \mathbf{x}_A, -t)$, from which $\bar{G}(\mathbf{x}_B, \mathbf{x}_A, t)$ and $G(\mathbf{x}_B, \mathbf{x}_A, -t)$ can be obtained by extracting the causal and acausal part, respectively. Porter (1970), Esmersoy & Oristaglio (1988) and Oristaglio (1989) used an expression similar to equation (1) (without the bars) in optical holography, seismic migration and acoustic inverse scattering, respectively, see Thorbecke & Wapenaar (2007) and Halliday & Curtis (2010) for a further discussion on the relation between these different applications of equation (1).

Next, we consider a convolution-type representation for the Green's function. We slightly modify the configuration by taking $\mathbf{x}_A$ outside $\mathbb{S}$ and renaming it $\mathbf{x}_S$, see Figure 1b. For this configuration the convolution-type representation is given by

$$\hat{G}(\mathbf{x}_B, \mathbf{x}_S, \omega) = \qquad (2)$$
$$-\oint_{\mathbb{S}} \frac{1}{j\omega\rho(\mathbf{x})} \Big(\partial_i \hat{\bar{G}}(\mathbf{x}_B, \mathbf{x}, \omega) \hat{G}(\mathbf{x}, \mathbf{x}_S, \omega)$$
$$-\hat{\bar{G}}(\mathbf{x}_B, \mathbf{x}, \omega) \partial_i \hat{G}(\mathbf{x}, \mathbf{x}_S, \omega) \Big) n_i \, \mathrm{d}\mathbf{x}.$$

Due to the absence of complex conjugation signs, the products on the right-hand side correspond to crossconvolutions in the time domain. An important difference with the correlation-type representation is that this representation remains valid in media with losses. Again, the bar in $\hat{\bar{G}}$ refers to a reference state with possibly different boundary conditions at $\mathbb{S}$ and/or different medium parameters outside $\mathbb{S}$.

Slob & Wapenaar (2007) use the electromagnetic equivalent of equation (2) (without the bars) as the starting point for interferometry by crossconvolution in lossy media. A discussion of interferometry by crossconvolution is beyond the scope of this paper. We will use equation (2) as the starting point for interferometry by deconvolution in open systems. By considering $\hat{\bar{G}}(\mathbf{x}_B, \mathbf{x}, \omega)$ under the integral as the unknown quantity, equation (2) needs to be resolved by multi-dimensional deconvolution.

3 BASIC ASPECTS OF INTERFEROMETRY BY CROSSCORRELATION

3.1 Simplification of the integral

The correlation-type Green's function representation (equation 1) is the basic expression for seismic interferometry by crosscorrelation in open systems. The right-hand side of this equation contains a combination of two correlation products. We show how we can combine these two terms into a single term. To this end, we assume that the medium at and outside $\mathbb{S}$ is homogeneous, with constant propagation velocity c and mass density ρ, for $\hat{G}$ as well as for $\hat{\bar{G}}$. In other words, $\mathbb{S}$ is an absorbing boundary for $\hat{G}$ and $\hat{\bar{G}}$. Because the boundary conditions are the same, we drop the bar in $\hat{\bar{G}}$ in the remainder of this section. Assuming $\mathbb{S}$ is sufficiently smooth, the normal differential operator $n_i\partial_i$ acting on the Green's functions can be replaced by a pseudo-differential operator $-j\hat{\mathcal{H}}_1$, where $\hat{\mathcal{H}}_1$ is the square-root of the Helmholtz operator defined on curvilinear coordinates along $\mathbb{S}$. For details about this operator we refer to Fishman & McCoy (1984), Wapenaar & Berkhout (1989, Appendix B), Fishman (1993), and Frijlink & Wapenaar (2010). Hence, for the integral in equation (1) we may write

$$\oint_{\mathbb{S}} \Big((\partial_i \hat{G}_B) \hat{G}_A^* - \hat{G}_B (\partial_i \hat{G}_A^*) \Big) n_i \, \mathrm{d}\mathbf{x} = \qquad (3)$$
$$\oint_{\mathbb{S}} \Big((-j\hat{\mathcal{H}}_1 \hat{G}_B) \hat{G}_A^* - \hat{G}_B (j\hat{\mathcal{H}}_1^* \hat{G}_A^*) \Big) \mathrm{d}\mathbf{x} =$$
$$\oint_{\mathbb{S}} (-j(\hat{\mathcal{H}}_1 + \hat{\mathcal{H}}_1^*) \hat{G}_B) \hat{G}_A^* \, \mathrm{d}\mathbf{x},$$

where we used the fact that $\hat{\mathcal{H}}_1$ is symmetric [in the sense that $\oint (\hat{\mathcal{H}}_1 f) g \, \mathrm{d}\mathbf{x} = \oint f (\hat{\mathcal{H}}_1 g) \, \mathrm{d}\mathbf{x}$]. Note that $\hat{G}_A$ and $\hat{G}_B$ stand for $\hat{G}(\mathbf{x}_A, \mathbf{x}, \omega)$ and $\hat{G}(\mathbf{x}_B, \mathbf{x}, \omega)$, respectively. Zheng (2010) and Zheng et al. (2011) evaluate the kernel of $-j(\hat{\mathcal{H}}_1 + \hat{\mathcal{H}}_1^*)$ analytically for a number of special cases and show that in theory this may lead to an exact retrieval of the Green's function. For most practical applications some further approximations need to be made. If we ignore the contribution of evanescent waves, we may approximate $\hat{\mathcal{H}}_1^*$ by $\hat{\mathcal{H}}_1$, hence

$$\oint_{\mathbb{S}} (-j(\hat{\mathcal{H}}_1 + \hat{\mathcal{H}}_1^*) \hat{G}_B) \hat{G}_A^* \, \mathrm{d}\mathbf{x} \approx$$
$$2 \oint_{\mathbb{S}} (-j\hat{\mathcal{H}}_1 \hat{G}_B) \hat{G}_A^* \, \mathrm{d}\mathbf{x} = 2 \oint_{\mathbb{S}} (n_i \partial_i \hat{G}_B) \hat{G}_A^* \, \mathrm{d}\mathbf{x}. \quad (4)$$

~~In the high-frequency regime, the derivatives of these Green's functions can be approximated by multiplying each constituent (direct wave, scattered wave, etc.) by $-jk|\cos\alpha|$, where $k = \omega/c$, and α is the angle between the~~

~~relevant ray and the normal on S. The main contributions to the integral in equation (1) come from stationary points on S. At those points the ray angles for $\hat{G}$ and $\hat{\bar{G}}$ are identical (for a simple proof, see the Appendix in Wapenaar et al. (2010a)). Hence, at each stationary point we can simplify the integrand of equation (1) as follows~~

$$~~\left((\partial_i\hat{\bar{G}})\hat{G}^* - \hat{\bar{G}}(\partial_i\hat{G}^*)\right)n_i =~~$$
$$~~-jk|\cos\alpha|\left(\hat{\bar{G}}\hat{G}^* - \hat{\bar{G}}(-\hat{G}^*)\right) =~~$$
$$~~-2jk|\cos\alpha|\hat{\bar{G}}\hat{G}^* = 2(n_i\partial_i\hat{\bar{G}})\hat{G}^*.~~$$

Using equations (3) and (4) in equation (1) and rewriting $\mathbf{x}$ as $\mathbf{x}_S$ (standing for the source coordinate vector), ~~and dropping the bars (because we considered the same boundary conditions for $\hat{G}$ and $\hat{\bar{G}}$),~~ we obtain

$$\hat{G}(\mathbf{x}_B,\mathbf{x}_A,\omega) + \hat{G}^*(\mathbf{x}_B,\mathbf{x}_A,\omega) = \qquad (5)$$
$$-\frac{2}{j\omega\rho}\oint_{\mathbb{S}_{\mathrm{src}}}\left(n_i\partial_i^S\hat{G}(\mathbf{x}_B,\mathbf{x}_S,\omega)\right)\hat{G}^*(\mathbf{x}_A,\mathbf{x}_S,\omega)\,\mathrm{d}\mathbf{x}_S,$$

where the superscript S in ∂_i^S denotes that the differentiation is carried out with respect to the components of $\mathbf{x}_S$. Note that we added a subscript 'src' in $\mathbb{S}_{\mathrm{src}}$ to denote that the integration surface contains the sources of the Green's functions. The integrand of equation (5) contains a single crosscorrelation product of dipole and monopole source responses. When only monopole responses are available, the operation $n_i\partial_i^S$ can be replaced ~~by a pseudo-differential operator acting along $\mathbb{S}_{\mathrm{src}}$, or~~ in the high-frequency approximation by multiplications with $-jk|\cos\alpha|$, where $k=\omega/c$, and α is the angle between the relevant ray and the normal on $\mathbb{S}$ at the stationary points. ~~when the ray angles are known.~~ Hence, for controlled-source interferometry, in which case the source positions are known and $\mathbb{S}_{\mathrm{src}}$ is usually a smooth surface, equation (5) is a useful expression. In passive interferometry, the positions of the sources are unknown and $\mathbb{S}_{\mathrm{src}}$ can be very irregular. In that case the best one can do is ~~to~~ replace the operation $n_i\partial_i^S$ by a factor $-jk$, which leads to

$$\hat{G}(\mathbf{x}_B,\mathbf{x}_A,\omega) + \hat{G}^*(\mathbf{x}_B,\mathbf{x}_A,\omega) \approx \qquad (6)$$
$$\frac{2}{\rho c}\oint_{\mathbb{S}_{\mathrm{src}}}\hat{G}(\mathbf{x}_B,\mathbf{x}_S,\omega)\hat{G}^*(\mathbf{x}_A,\mathbf{x}_S,\omega)\,\mathrm{d}\mathbf{x}_S.$$

Equation (6) is accurate when $\mathbb{S}_{\mathrm{src}}$ is a sphere with a very large radius, but it involves amplitude errors when $\mathbb{S}_{\mathrm{src}}$ is finite. Moreover, spurious events may occur due to incomplete cancelation of contributions from different stationary points. However, since the approximation does not affect the phase, equation (6) is usually considered acceptable for seismic interferometry. Note that for a modified Green's function $\hat{\mathcal{G}} = \hat{G}/j\omega$ we have, instead of equation (6),

$$\hat{\mathcal{G}}(\mathbf{x}_B,\mathbf{x}_A,\omega) - \hat{\mathcal{G}}^*(\mathbf{x}_B,\mathbf{x}_A,\omega) \approx \qquad (7)$$
$$-\frac{2j\omega}{\rho c}\oint_{\mathbb{S}_{\mathrm{src}}}\hat{\mathcal{G}}(\mathbf{x}_B,\mathbf{x}_S,\omega)\hat{\mathcal{G}}^*(\mathbf{x}_A,\mathbf{x}_S,\omega)\,\mathrm{d}\mathbf{x}_S$$

(Wapenaar & Fokkema 2006). Both equations (6) and (7) are used in the literature on seismic interferometry. Because of the simple relation between $\hat{G}$ and $\hat{\mathcal{G}}$, these equations are completely interchangeable. In the following we continue

with equation (6). In the time domain this equation reads

$$G(\mathbf{x}_B,\mathbf{x}_A,t) + G(\mathbf{x}_B,\mathbf{x}_A,-t) \approx \qquad (8)$$
$$\frac{2}{\rho c}\oint_{\mathbb{S}_{\mathrm{src}}}G(\mathbf{x}_B,\mathbf{x}_S,t) * G(\mathbf{x}_A,\mathbf{x}_S,-t)\,\mathrm{d}\mathbf{x}_S.$$

The in-line asterisk $*$ denotes temporal convolution, but the time-reversal of the second Green's function turns the convolution into a correlation. Equation (8) shows that the crosscorrelation of two Green's functions observed by receivers at $\mathbf{x}_A$ and $\mathbf{x}_B$, followed by an integration along the sources, gives the Green's function between $\mathbf{x}_A$ and $\mathbf{x}_B$ plus its time-reversed version.

3.2   Transient and noise sources

For practical situations the Green's functions in the right-hand side of equation (8) should be replaced by responses of real sources, i.e., Green's functions convolved with source functions. When the source functions are transients, $s(\mathbf{x}_S,t)$, we write for the responses at $\mathbf{x}_A$ and $\mathbf{x}_B$

$$u(\mathbf{x}_A,\mathbf{x}_S,t) = G(\mathbf{x}_A,\mathbf{x}_S,t) * s(\mathbf{x}_S,t), \qquad (9)$$
$$u(\mathbf{x}_B,\mathbf{x}_S,t) = G(\mathbf{x}_B,\mathbf{x}_S,t) * s(\mathbf{x}_S,t). \qquad (10)$$

For this situation, we define a correlation function $C(\mathbf{x}_B,\mathbf{x}_A,t)$ as

$$C(\mathbf{x}_B,\mathbf{x}_A,t) = \oint_{\mathbb{S}_{\mathrm{src}}}\mathcal{F}(\mathbf{x}_S,t)*u(\mathbf{x}_B,\mathbf{x}_S,t)*u(\mathbf{x}_A,\mathbf{x}_S,-t)\,\mathrm{d}\mathbf{x}_S,$$
$$(11)$$

where $\mathcal{F}(\mathbf{x}_S,t)$ is a filter that compensates for the variations of the autocorrelation of the source function, in such a way that

$$\mathcal{F}(\mathbf{x}_S,t) * s(\mathbf{x}_S,t) * s(\mathbf{x}_S,-t) = S(t), \qquad (12)$$

where $S(t)$ is some (arbitrarily chosen) average autocorrelation. Substituting equations (9) and (10) into equation (11), using equation (12) and comparing the result with equation (8) gives

$$\{G(\mathbf{x}_B,\mathbf{x}_A,t) + G(\mathbf{x}_B,\mathbf{x}_A,-t)\} * S(t) \approx \frac{2}{\rho c}C(\mathbf{x}_B,\mathbf{x}_A,t).$$
$$(13)$$

When the source functions are simultaneously acting noise signals, $N(\mathbf{x}_S,t)$, the responses at $\mathbf{x}_A$ and $\mathbf{x}_B$ are given by

$$u(\mathbf{x}_A,t) = \oint_{\mathbb{S}_{\mathrm{src}}}G(\mathbf{x}_A,\mathbf{x}_S,t) * N(\mathbf{x}_S,t)\,\mathrm{d}\mathbf{x}_S, \quad (14)$$
$$u(\mathbf{x}_B,t) = \oint_{\mathbb{S}_{\mathrm{src}}}G(\mathbf{x}_B,\mathbf{x}_S',t) * N(\mathbf{x}_S',t)\,\mathrm{d}\mathbf{x}_S'. \quad (15)$$

We assume that two noise sources $N(\mathbf{x}_S,t)$ and $N(\mathbf{x}_S',t)$ are mutually uncorrelated for any $\mathbf{x}_S \neq \mathbf{x}_S'$ on $\mathbb{S}_{\mathrm{src}}$ and that their autocorrelations are independent of $\mathbf{x}_S$. Hence, we assume that these noise sources obey the relation

$$\langle N(\mathbf{x}_S',t) * N(\mathbf{x}_S,-t)\rangle = \delta(\mathbf{x}_S - \mathbf{x}_S')S(t), \qquad (16)$$

where $\langle\cdot\rangle$ denotes ensemble averaging and $S(t)$ the autocorrelation of the noise. Note that $\delta(\mathbf{x}_S - \mathbf{x}_S')$ is defined for $\mathbf{x}_S$ and $\mathbf{x}_S'$ both on $\mathbb{S}_{\mathrm{src}}$. This time we define the correlation function as

$$C(\mathbf{x}_B,\mathbf{x}_A,t) = \langle u(\mathbf{x}_B,t) * u(\mathbf{x}_A,-t)\rangle. \qquad (17)$$
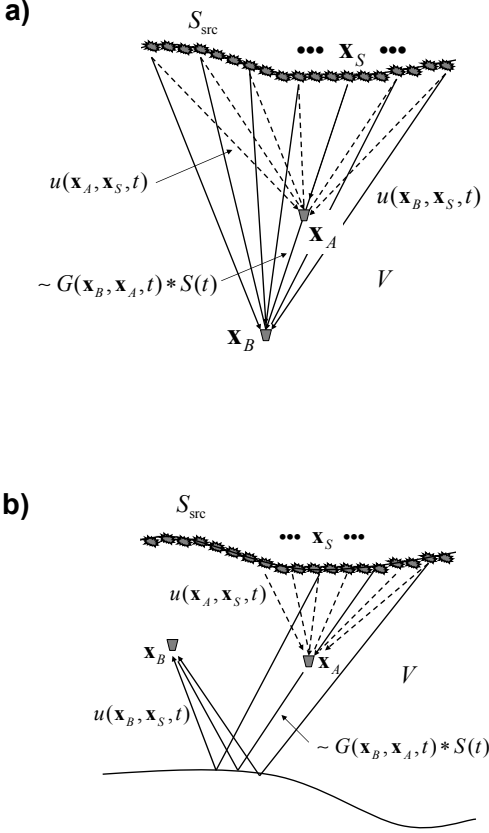
Figure 2. *(a) Illustration of interferometry by crosscorrelation (equations (11) and (13)) for the situation of direct-wave interferometry. The responses $u(\mathbf{x}_A, \mathbf{x}_S, t)$ and $u(\mathbf{x}_B, \mathbf{x}_S, t)$ are crosscorrelated and the results for all sources $\mathbf{x}_S$ are integrated along the source boundary $\mathbb{S}_{\mathrm{src}}$. The correlation function is approximately proportional to $G(\mathbf{x}_B, \mathbf{x}_A, t) * S(t)$. (b) Idem, for reflected-wave interferometry.*

In practice, the ensemble averaging is replaced by integrating over sufficiently long time and/or averaging over different time intervals. Substituting equations (14) and (15) into equation (17), using equation (16) and comparing the result with equation (8) gives again equation (13). Hence, whether we consider transient or noise sources, equation (13) states that a properly defined correlation function gives the Green's function plus its time-reversed version, convolved with the autocorrelation of the source function.

In most practical situations, sources are not available on a closed boundary. When a part of the integration boundary is a free surface, the integrals need only be evaluated over the remaining part of the boundary, hence, sources need only be available on an open boundary $\mathbb{S}_{\mathrm{src}}$ that, together with the free surface, forms a closed boundary. This situation occurs in passive reflected-wave interferometry (section 6.2). In many other situations the closed source boundary is replaced by an open surface, simply because the available source aperture is restricted to an open boundary. This is

illustrated in Figure 2a for the situation of direct-wave interferometry and in Figure 2b for controlled-source reflected-wave interferometry (these configurations will be discussed in more detail in sections 6.1 and 5.1, respectively). Since the underlying representation (equation 1) is of the correlation type (in which one of the Green's functions is backward propagating), radiation conditions do not apply anywhere on $\mathbb{S}$, hence, replacing the closed surface by an open surface necessarily leads to approximations. For the situation of direct-wave interferometry (Figure 2a) the main effect is that the correlation function $C(\mathbf{x}_B, \mathbf{x}_A, t)$ is approximately proportional to $G(\mathbf{x}_B, \mathbf{x}_A, t) * S(t)$, i.e, the time-reversed version of the Green's function in equation (13) is not recovered (see e.g. Miyazawa et al. (2008)). For reflected-wave interferometry (Figure 2b), one-sided illumination can lead to severe distortions of the retrieved Green's function. Moreover, Snieder et al. (2006b) show that even for very simple configurations it may lead to spurious multiples. A partial solution, implemented by Bakulin & Calvert (2006), is the application of a time window to $u(\mathbf{x}_A, \mathbf{x}_S, t)$ in equation (11), with the aim of selecting direct waves only. Another approach is up/down decomposition. Figure 2b suggests to replace the total fields $u(\mathbf{x}_A, \mathbf{x}_S, t)$ and $u(\mathbf{x}_B, \mathbf{x}_S, t)$ by downward and upward propagating fields $u^+(\mathbf{x}_A, \mathbf{x}_S, t)$ and $u^-(\mathbf{x}_B, \mathbf{x}_S, t)$ (of course this decomposition requires that multi-component data are available). With this decomposition, equation (11) could be replaced by

$$C(\mathbf{x}_B, \mathbf{x}_A, t) =$$
$$\int_{\mathbb{S}_{\mathrm{src}}} \mathcal{F}(\mathbf{x}_S, t) * u^-(\mathbf{x}_B, \mathbf{x}_S, t) * u^+(\mathbf{x}_A, \mathbf{x}_S, -t) \, \mathrm{d}\mathbf{x}_S, \quad (18)$$

with $C(\mathbf{x}_B, \mathbf{x}_A, t)$ approximately proportional to $G(\mathbf{x}_B, \mathbf{x}_A, t) * S(t)$. This approach is followed by Mehta et al. (2007a) and van der Neut & Wapenaar (2009), who show that decomposition prior to crosscorrelation indeed leads to a reduction of the spurious multiples. Nevertheless, also the application of equation (18) does not lead to an undistorted recovery of the Green's function. An important aspect of interferometry by MDD, discussed in the next section, is that the approximations of one-sided illumination are avoided in a natural way.

4 BASIC ASPECTS OF INTERFEROMETRY BY MULTI-DIMENSIONAL DECONVOLUTION (MDD)

4.1 Simplification of the integral

The convolution-type Green's function representation (equation 2) is the basic expression for seismic interferometry by multi-dimensional deconvolution in open systems. The right-hand side of this equation contains a combination of two convolution products. We show how we can combine these two terms into a single term. The Green's function $\hat{\bar{G}}(\mathbf{x}_B, \mathbf{x}, \omega)$ under the integral is the unknown that we want to resolve by MDD. The Green's function $\hat{G}(\mathbf{x}_B, \mathbf{x}_S, \omega)$ on the left-hand side and $\hat{G}(\mathbf{x}, \mathbf{x}_S, \omega)$ under the integral are related to the observations. Hence, $\hat{G}$ is defined in the actual medium inside as well as outside $\mathbb{S}$, but for $\hat{\bar{G}}$ we are free to choose convenient boundary conditions at $\mathbb{S}$. In the following we let $\mathbb{S}$ be an absorbing boundary for $\hat{\bar{G}}(\mathbf{x}_B, \mathbf{x}, \omega) = \hat{\bar{G}}(\mathbf{x}, \mathbf{x}_B, \omega)$,

so that $\hat{\bar{G}}(\mathbf{x}, \mathbf{x}_B, \omega)$ is outward propagating at $\mathbb{S}$. Furthermore, we write $\hat{G}(\mathbf{x}, \mathbf{x}_S, \omega)$ as the superposition of an inward and outward propagating part at $\mathbf{x}$ on $\mathbb{S}$, according to $\hat{G}(\mathbf{x}, \mathbf{x}_S, \omega) = \hat{G}^{\text{in}}(\mathbf{x}, \mathbf{x}_S, \omega) + \hat{G}^{\text{out}}(\mathbf{x}, \mathbf{x}_S, \omega)$. Assuming $\mathbb{S}$ is sufficiently smooth, we replace the differential operator $n_i \partial_i$ again by a pseudo-differential operator $\pm j\hat{\mathcal{H}}_1$, this time for a medium with losses (Wapenaar et al. 2001). The plus- and minus-sign in $\pm j\hat{\mathcal{H}}_1$ correspond to inward and outward propagating waves, respectively. Hence, we may write for the integral in equation (2), using the fact that $\hat{\mathcal{H}}_1$ is symmetric,

$$\oint_{\mathbb{S}} \Big((\partial_i \hat{\bar{G}}_B)(\hat{G}_S^{\text{in}} + \hat{G}_S^{\text{out}}) - \hat{\bar{G}}_B \partial_i (\hat{G}_S^{\text{in}} + \hat{G}_S^{\text{out}}) \Big) n_i \, d\mathbf{x} =$$

$$\oint_{\mathbb{S}} \Big((-j\hat{\mathcal{H}}_1 \hat{\bar{G}}_B)(\hat{G}_S^{\text{in}} + \hat{G}_S^{\text{out}}) - \hat{\bar{G}}_B j\hat{\mathcal{H}}_1 (\hat{G}_S^{\text{in}} - \hat{G}_S^{\text{out}}) \Big) d\mathbf{x} =$$

$$2 \oint_{\mathbb{S}} (-j\hat{\mathcal{H}}_1 \hat{\bar{G}}_B)\hat{G}_S^{\text{in}} \, d\mathbf{x} = 2 \oint_{\mathbb{S}} (n_i \partial_i \hat{\bar{G}}_B)\hat{G}_S^{\text{in}} \, d\mathbf{x}, \qquad (19)$$

where $\hat{G}_S^{\text{in/out}}$ and $\hat{\bar{G}}_B$ stand for $\hat{G}^{\text{in/out}}(\mathbf{x}, \mathbf{x}_S, \omega)$ and $\hat{\bar{G}}(\mathbf{x}_B, \mathbf{x}, \omega)$, respectively.

~~In the high-frequency regime, the derivatives are approximated by multiplying each constituent with $\pm jk|\cos\alpha|$. The main contributions come from stationary points on $\mathbb{S}$, which are different for terms containing $\hat{G}^{\text{in}}$ than for those containing $\hat{G}^{\text{out}}$. For terms containing $\hat{G}^{\text{in}}$ we have at the stationary points~~

~~$\Big((\partial_i \hat{\bar{G}})\hat{G}^{\text{in}} - \hat{\bar{G}}(\partial_i \hat{G}^{\text{in}}) \Big) n_i =$~~

~~$-jk|\cos\alpha| \Big(\hat{\bar{G}}\hat{G}^{\text{in}} - \hat{\bar{G}}(-\hat{G}^{\text{in}}) \Big) =$~~

~~$-2jk|\cos\alpha|\hat{\bar{G}}\hat{G}^{\text{in}} = 2(n_i \partial_i \hat{\bar{G}})\hat{G}^{\text{in}},$~~

~~whereas for terms containing $\hat{G}^{\text{out}}$ we have~~

~~$\Big((\partial_i \hat{\bar{G}})\hat{G}^{\text{out}} - \hat{\bar{G}}(\partial_i \hat{G}^{\text{out}}) \Big) n_i =$~~

~~$-jk|\cos\alpha| \Big(\hat{\bar{G}}\hat{G}^{\text{out}} - \hat{\bar{G}}\hat{G}^{\text{out}} \Big) = 0.$~~

Using this in equation (2), assuming ρ is constant on $\mathbb{S}$, we obtain

$$\hat{G}(\mathbf{x}_B, \mathbf{x}_S, \omega) =$$
$$\frac{-2}{j\omega\rho} \oint_{\mathbb{S}_{\text{rec}}} \big(n_i \partial_i \hat{\bar{G}}(\mathbf{x}_B, \mathbf{x}, \omega) \big) \hat{G}^{\text{in}}(\mathbf{x}, \mathbf{x}_S, \omega) \, d\mathbf{x}. \qquad (20)$$

We added a subscript 'rec' in $\mathbb{S}_{\text{rec}}$ to denote that the integration surface contains the receivers of the Green's function $\hat{G}^{\text{in}}$. For convenience we introduce a dipole Green's function, defined as

$$\hat{\bar{G}}_{\text{d}}(\mathbf{x}_B, \mathbf{x}, \omega) = \frac{-2}{j\omega\rho} \big(n_i \partial_i \hat{\bar{G}}(\mathbf{x}_B, \mathbf{x}, \omega) \big), \qquad (21)$$

so that equation (20) simplifies to

$$\hat{G}(\mathbf{x}_B, \mathbf{x}_S, \omega) = \oint_{\mathbb{S}_{\text{rec}}} \hat{\bar{G}}_{\text{d}}(\mathbf{x}_B, \mathbf{x}, \omega) \hat{G}^{\text{in}}(\mathbf{x}, \mathbf{x}_S, \omega) \, d\mathbf{x}. \qquad (22)$$

In the underlying representation (equation 2) it was assumed that $\mathbf{x}_B$ lies in $\mathbb{V}$. In several applications of MDD $\mathbf{x}_B$ is a receiver on $\mathbb{S}_{\text{rec}}$. For those applications we take $\mathbf{x}_B$ just inside $\mathbb{S}_{\text{rec}}$ to avoid several subtleties of taking $\mathbf{x}_B$ on $\mathbb{S}_{\text{rec}}$. In those applications it is often useful to consider only the outward propagating part of the field at $\mathbf{x}_B$. Applying decomposition at both sides of equation (22) gives

$$\hat{G}^{\text{out}}(\mathbf{x}_B, \mathbf{x}_S, \omega) = \oint_{\mathbb{S}_{\text{rec}}} \hat{\bar{G}}_{\text{d}}^{\text{out}}(\mathbf{x}_B, \mathbf{x}, \omega) \hat{G}^{\text{in}}(\mathbf{x}, \mathbf{x}_S, \omega) \, d\mathbf{x}. \qquad (23)$$

Equation (23) is nearly the same (except for a different normalization) as our previously derived one-way representation for MDD (Wapenaar et al. 2008a). In the following we continue with the notation of equation (22), where $\hat{G}(\mathbf{x}_B, \mathbf{x}_S, \omega)$ and $\hat{\bar{G}}_{\text{d}}(\mathbf{x}_B, \mathbf{x}, \omega)$ may stand for the total or the outward propagating fields at $\mathbf{x}_B$, depending on the application. In most practical situations, receivers are not available on a closed boundary, so the integration in equation (22) is necessarily restricted to an open receiver boundary $\mathbb{S}_{\text{rec}}$. As long as the source position $\mathbf{x}_S$ is located ~~on one~~ at the appropriate side of $\mathbb{S}_{\text{rec}}$ (i.e., outside $\mathbb{V}$), it suffices to take the integral over this open receiver boundary: since the underlying representation (equation 2) is of the convolution type, radiation conditions apply on the half-sphere that closes the boundary (assuming the half-sphere boundary is absorbing and its radius is sufficiently large), meaning that the contribution of the integral over that half-sphere vanishes. Hence, in the following we replace the closed boundary integral by an open boundary integral. In the time domain equation (22) thus becomes

$$G(\mathbf{x}_B, \mathbf{x}_S, t) = \int_{\mathbb{S}_{\text{rec}}} \bar{G}_{\text{d}}(\mathbf{x}_B, \mathbf{x}, t) * G^{\text{in}}(\mathbf{x}, \mathbf{x}_S, t) \, d\mathbf{x}. \qquad (24)$$

Unlike the correlation-type representation (equation 8), which holds under the condition that $\mathbb{S}_{\text{src}}$ is a closed surface with very large radius, the convolution-type representation of equation (24) holds as long as the open surface $\mathbb{S}_{\text{rec}}$ is sufficiently smooth and $\mathbf{x}_B$ and $\mathbf{x}_S$ lie at opposite sides of $\mathbb{S}_{\text{rec}}$. Moreover, whereas equation (8) only holds for lossless media, equation (24) also holds in media with losses. Equation (24) is an implicit representation of the convolution type for $\bar{G}_{\text{d}}(\mathbf{x}_B, \mathbf{x}, t)$. If it were a single equation, the inverse problem would be ill-posed. However, equation (24) holds for each source position $\mathbf{x}_S$ (outside $\mathbb{V}$), which we will denote from hereon by $\mathbf{x}_S^{(i)}$, where i denotes the source number. Solving the ensemble of equations for $\bar{G}_{\text{d}}(\mathbf{x}_B, \mathbf{x}, t)$ involves MDD.

4.2   Transient sources

For practical applications the Green's functions G and G^{in} in equation (24) should be replaced by responses of real sources, i.e., Green's functions convolved with source functions. For transient sources we may write for the responses at $\mathbf{x}$ and $\mathbf{x}_B$

$$u^{\text{in}}(\mathbf{x}, \mathbf{x}_S^{(i)}, t) = G^{\text{in}}(\mathbf{x}, \mathbf{x}_S^{(i)}, t) * s^{(i)}(t), \qquad (25)$$

$$u(\mathbf{x}_B, \mathbf{x}_S^{(i)}, t) = G(\mathbf{x}_B, \mathbf{x}_S^{(i)}, t) * s^{(i)}(t). \qquad (26)$$

Hence, by convolving both sides of equation (24) with $s^{(i)}(t)$ we obtain

$$u(\mathbf{x}_B, \mathbf{x}_S^{(i)}, t) = \int_{\mathbb{S}_{\text{rec}}} \bar{G}_{\text{d}}(\mathbf{x}_B, \mathbf{x}, t) * u^{\text{in}}(\mathbf{x}, \mathbf{x}_S^{(i)}, t) \, d\mathbf{x}. \qquad (27)$$

Here $u(\mathbf{x}_B, \mathbf{x}_S^{(i)}, t)$ and $\bar{G}_{\text{d}}(\mathbf{x}_B, \mathbf{x}, t)$ may stand for the total or the outward propagating fields at $\mathbf{x}_B$. We discuss the modifications for noise sources in section 4.4 and for simultaneous source acquisition in section 4.5.

Equation (27) is illustrated in Figure 3a for the situation of direct-wave interferometry and in Figure 3b for reflected-wave interferometry (with superscripts "out" added). Note that we consider the sources to be irregularly distributed in
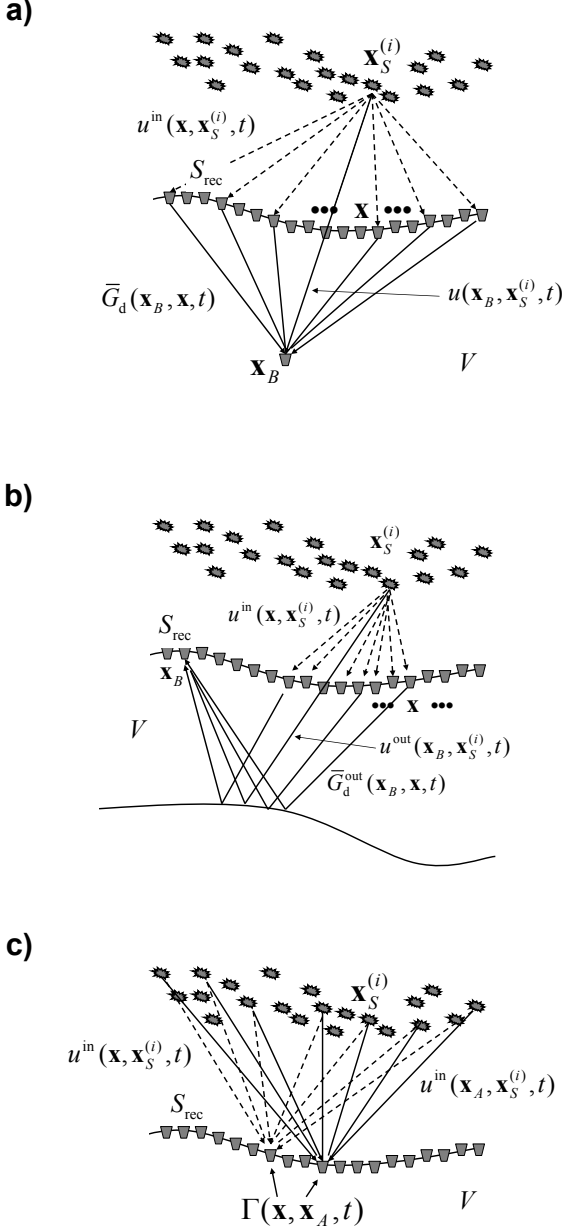
space. This is possible because equation (27) holds for each source separately whereas the integration is performed along the receivers. The configurations in Figures 3a and b will be discussed in more detail in sections 6.1 and 5.

Although in the derivation of equation (27) we tacitly assumed a point source of volume injection rate at $\mathbf{x}_S^{(i)}$, equation (27) holds equally well for other types of sources at $\mathbf{x}_S^{(i)}$, such as volume force or dislocation sources. The source also is not necessarily a point source. For an extended source, both sides of equation (27) can be integrated along the extended source, yielding an equation with exactly the same form, but with $u^{\mathrm{in}}(\mathbf{x}, \mathbf{x}_S^{(i)}, t)$ and $u(\mathbf{x}_B, \mathbf{x}_S^{(i)}, t)$ being the responses of the extended source.

4.3 Relation with the correlation method

Solving equation (27) in a least-squares sense is equivalent to solving its normal equation (Menke 1989). We obtain the normal equation by crosscorrelating both sides of equation (27) with $u^{\mathrm{in}}(\mathbf{x}_A, \mathbf{x}_S^{(i)}, t)$ (with $\mathbf{x}_A$ on $\mathbb{S}_{\mathrm{rec}}$) and taking the sum over all sources (van der Neut et al. 2010). This gives

$$C(\mathbf{x}_B, \mathbf{x}_A, t) = \int_{\mathbb{S}_{\mathrm{rec}}} \bar{G}_{\mathrm{d}}(\mathbf{x}_B, \mathbf{x}, t) * \Gamma(\mathbf{x}, \mathbf{x}_A, t)\ \mathrm{d}\mathbf{x}, \quad (28)$$

where

$$
\begin{aligned}
C(\mathbf{x}_B, \mathbf{x}_A, t) & \qquad\qquad\qquad\qquad (29)\\
&= \sum_i u(\mathbf{x}_B, \mathbf{x}_S^{(i)}, t) * u^{\mathrm{in}}(\mathbf{x}_A, \mathbf{x}_S^{(i)}, -t)\\
&= \sum_i G(\mathbf{x}_B, \mathbf{x}_S^{(i)}, t) * G^{\mathrm{in}}(\mathbf{x}_A, \mathbf{x}_S^{(i)}, -t) * S^{(i)}(t),
\end{aligned}
$$

$$
\begin{aligned}
\Gamma(\mathbf{x}, \mathbf{x}_A, t) & \qquad\qquad\qquad\qquad (30)\\
&= \sum_i u^{\mathrm{in}}(\mathbf{x}, \mathbf{x}_S^{(i)}, t) * u^{\mathrm{in}}(\mathbf{x}_A, \mathbf{x}_S^{(i)}, -t)\\
&= \sum_i G^{\mathrm{in}}(\mathbf{x}, \mathbf{x}_S^{(i)}, t) * G^{\mathrm{in}}(\mathbf{x}_A, \mathbf{x}_S^{(i)}, -t) * S^{(i)}(t),
\end{aligned}
$$

with

$$S^{(i)}(t) = s^{(i)}(t) * s^{(i)}(-t). \quad (31)$$

Equation (28) shows that the correlation function $C(\mathbf{x}_B, \mathbf{x}_A, t)$ is proportional to the sought Green's function $\bar{G}_{\mathrm{d}}(\mathbf{x}_B, \mathbf{x}, t)$ with its source smeared in space and time by $\Gamma(\mathbf{x}, \mathbf{x}_A, t)$.

Note that $C(\mathbf{x}_B, \mathbf{x}_A, t)$ as defined in equation (29) is a correlation function with a similar form as the one defined in equation (11). There are also some notable differences. In equation (11) an integration takes place along the source boundary $\mathbb{S}_{\mathrm{src}}$, whereas equation (29) involves a summation over individual sources. Of course in practical situations the integral in equation (11) needs to be replaced by a summation as well, but this should be done carefully, obeying the common restrictions for discretization of continuous integrands. On the other hand, the summation in equation (29) simply takes place over the available sources and as such puts no restrictions on the regularity of the source distribution. We will hold on to the integral notation in equation (11) versus the summation notation in equation (29) to express the differences in the assumptions on the regularity of the source distribution. The effect of this difference in

Figure 3. *(a) Illustration of the convolutional model (equation 27), underlying interferometry by MDD for the situation of direct-wave interferometry. The inward propagating field $u^{\mathrm{in}}(\mathbf{x}, \mathbf{x}_S^{(i)}, t)$ is convolved with $\bar{G}_{\mathrm{d}}(\mathbf{x}_B, \mathbf{x}, t)$ and the results for all receivers $\mathbf{x}$ are integrated along the receiver boundary $\mathbb{S}_{\mathrm{rec}}$, giving the response $u(\mathbf{x}_B, \mathbf{x}_S^{(i)}, t)$. Assuming equation (27) is available for many source positions $\mathbf{x}_S^{(i)}$, the Green's function $\bar{G}_{\mathrm{d}}(\mathbf{x}_B, \mathbf{x}, t)$ can be retrieved by MDD. (b) Idem, for reflected-wave interferometry, with $u(\mathbf{x}_B, \mathbf{x}_S^{(i)}, t)$ and $\bar{G}_{\mathrm{d}}(\mathbf{x}_B, \mathbf{x}, t)$ replaced by the outgoing fields $u^{\mathrm{out}}(\mathbf{x}_B, \mathbf{x}_S^{(i)}, t)$ and $\bar{G}_{\mathrm{d}}^{\mathrm{out}}(\mathbf{x}_B, \mathbf{x}, t)$, respectively. (c) Illustration of the point-spread function $\Gamma(\mathbf{x}, \mathbf{x}_A, t)$ (equation 30), defined as the crosscorrelation of the inward propagating fields at $\mathbf{x}$ and $\mathbf{x}_A$ on $\mathbb{S}_{\mathrm{rec}}$, summed over the sources. In the ideal case it is proportional to a band-limited delta function on $\mathbb{S}_{\mathrm{rec}}$, but in practice there are many factors that make it different from a delta function.*

assumptions will be illustrated in sections 6.1 and 6.2. Another difference is that in equation (11) the full wave fields at $\mathbf{x}_A$ and $\mathbf{x}_B$ are crosscorrelated, whereas in equation (29) the inward propagating part of the wavefield at $\mathbf{x}_A$ is crosscorrelated with the full (or outward propagating) wave field at $\mathbf{x}_B$. The final difference is the filter $\mathcal{F}(\mathbf{x}_S, t)$ in equation (11) which shapes the different autocorrelations of the different sources to an average autocorrelation function $S(t)$; in equation (29) this filter is not needed.

$\Gamma(\mathbf{x}, \mathbf{x}_A, t)$ as defined in equation (30) is the crosscorrelation of the inward propagating wave fields at $\mathbf{x}$ and $\mathbf{x}_A$, summed over the sources (van der Neut et al. 2010), see Figure 3c. We call $\Gamma(\mathbf{x}, \mathbf{x}_A, t)$ the space-time point-spread function. If we would have a regular distribution of sources with equal autocorrelation functions $S(t)$ along a large planar source boundary, and if the medium between the source and receiver boundaries were homogeneous and lossless, the point-spread function would approach a temporally and spatially band-limited delta function, see Appendix A for details. Hence, for this situation equation (28) merely states that the correlation function $C(\mathbf{x}_B, \mathbf{x}_A, t)$ is proportional to the response of a temporally and spatially band-limited source. ~~$\Gamma(\mathbf{x}, \mathbf{x}_A, t) \approx (\rho c/2)^2 \delta(\mathbf{x} - \mathbf{x}_A)S(t)$ [here $\delta(\mathbf{x} - \mathbf{x}_A)$ is defined for $\mathbf{x}$ and $\mathbf{x}_A$ both on $\mathbb{S}_{\text{rec}}$; the approximation sign accounts for the fact that even under these ideal circumstances the point-spread function is spatially band-limited because the correlation in equation (30) does not compensate for evanescent waves]. Hence, for this situation, equation (28) would simplify to $C(\mathbf{x}_B, \mathbf{x}_A, t) \approx (\rho c/2)^2 \bar{G}_{\text{d}}(\mathbf{x}_B, \mathbf{x}_A, t) * S(t)$, so the Green's function $\bar{G}_{\text{d}}(\mathbf{x}_B, \mathbf{x}_A, t)$ could be simply obtained by deconvolving the correlation function $C(\mathbf{x}_B, \mathbf{x}_A, t)$ for $S(t)$.~~ In practice, there are many factors that make the point-spread function $\Gamma(\mathbf{x}, \mathbf{x}_A, t)$ deviate from a band-limited delta function. Among these factors are simultaneous source acquisition (section 4.5), medium inhomogeneities (section 5.1), multiple reflections in the illuminating wavefield (section 5.2), intrinsic losses (section 5.3), irregularity of the source distribution (sections 6.1 and 6.2), etc. For all those cases equation (28) shows that the point-spread function blurs the source of the Green's function in the spatial directions and generates ghosts ("spurious multiples", Snieder et al. (2006b)) in the temporal direction. MDD involves inverting equation (28), see section 4.6. Ideally, this removes the distorting effects of the space-time point-spread function $\Gamma(\mathbf{x}, \mathbf{x}_A, t)$ from the correlation function $C(\mathbf{x}_B, \mathbf{x}_A, t)$ and yields an estimate of the Green's function $\bar{G}_{\text{d}}(\mathbf{x}_B, \mathbf{x}, t)$.

Note that the space-time point-spread function $\Gamma(\mathbf{x}, \mathbf{x}_A, t)$ plays a similar role in interferometry by MDD as the spatial point-spread function (or spatial resolution function) in optical, acoustical and seismic imaging systems (Born & Wolf 1965; Norton 1992; Miller et al. 1987; Schuster & Hu 2000; Gelius et al. 2002; Lecomte 2008; Toxopeus et al. 2008; van Veldhuizen et al. 2008). For example, in seismic migration the point-spread function is defined as the migration result of the response of a single point scatterer. It is a useful tool to assess migration results in relation with geological parameters, background model, acquisition parameters, etc. Moreover, it is sometimes used in migration deconvolution to improve the spatial resolution of the migration image (Hu et al. 2001; Yu et al. 2006). In a similar way, van der Neut & Thorbecke (2009) use the space-time

point-spread function $\Gamma(\mathbf{x}, \mathbf{x}_A, t)$ to assess the quality of the virtual source obtained by correlation-based interferometry. Moreover, analogous to migration deconvolution, interferometry by MDD (i.e., inversion of equation (28)) aims at deblurring and deghosting the virtual source. An important difference is that the interferometric space-time point-spread function is obtained from measured responses, whereas the spatial point-spread function used in migration deconvolution is modeled in a background medium. As a result, the interferometric point-spread function accounts much more accurately for the distorting effects of the medium inhomogeneities, including multiple scattering.

4.4   Noise sources

We show that equation (28) also holds for the situation of simultaneously acting uncorrelated noise sources. To this end, we define the correlation function and the point-spread function, respectively, as

$$C(\mathbf{x}_B, \mathbf{x}_A, t) = \langle u(\mathbf{x}_B, t) * u^{\text{in}}(\mathbf{x}_A, -t)\rangle, \qquad (32)$$

$$\Gamma(\mathbf{x}, \mathbf{x}_A, t) = \langle u^{\text{in}}(\mathbf{x}, t) * u^{\text{in}}(\mathbf{x}_A, -t)\rangle, \qquad (33)$$

where the noise responses are defined as

$$u^{\text{in}}(\mathbf{x}_A, t) = \sum_i G^{\text{in}}(\mathbf{x}_A, \mathbf{x}_S^{(i)}, t) * N^{(i)}(t), \qquad (34)$$

$$u^{\text{in}}(\mathbf{x}, t) = \sum_j G^{\text{in}}(\mathbf{x}, \mathbf{x}_S^{(j)}, t) * N^{(j)}(t), \qquad (35)$$

$$u(\mathbf{x}_B, t) = \sum_j G(\mathbf{x}_B, \mathbf{x}_S^{(j)}, t) * N^{(j)}(t), \qquad (36)$$

in which the noise signals are assumed to be mutually uncorrelated, according to

$$\langle N^{(j)}(t) * N^{(i)}(-t)\rangle = \delta_{ij}S^{(i)}(t). \qquad (37)$$

Upon substitution of equations $(34) - (36)$ into equations (32) and (33), using equation (37), it follows that the correlation function and the point-spread function as defined in equations (32) and (33) are identical to those defined in equations (29) and (30). Hence, whether we consider transient or noise sources, equation (28) is the relation that needs to be inverted by MDD to resolve the Green's function $\bar{G}_{\text{d}}(\mathbf{x}_B, \mathbf{x}, t)$.

Note that the correlation function $C(\mathbf{x}_B, \mathbf{x}_A, t)$ as defined in equation (32) resembles that defined in equation (17). There are again three main differences. Equation (17) is the correlation of noise responses which are defined as integrals over sources on $\mathbb{S}_{\text{src}}$ (equations 14 and 15), whereas the correlated responses in equation (32) are defined as summations over individual sources (equations 34 and 36). As mentioned before, this reflects the difference in assumptions on the regularity of the source distribution (see sections 6.1 and 6.2). Furthermore, in equation (17) the full noise fields at $\mathbf{x}_A$ and $\mathbf{x}_B$ are crosscorrelated, whereas in equation (32) the inward propagating part of the noise field at $\mathbf{x}_A$ is crosscorrelated with the full (or outward propagating) noise field at $\mathbf{x}_B$. Finally, an underlying assumption of equation (17) is that the noise sources all have the same autocorrelation function $S(t)$ (equation 16), whereas equation (32) is still valid when the autocorrelations of the different sources are different from one another (equation 37).

4.5 Simultaneous source acquisition (or "blended acquisition")

A new trend in the seismic exploration community is simultaneous source acquisition, also known as blended acquisition (Beasley et al. 1998; Bagaini 2006; Ikelle 2007; Stefani et al. 2007; Howe et al. 2007; Hampson et al. 2008; Berkhout 2008). Seismic sources are fired with relatively small intervals to reduce the total acquisition time. As a result, the seismic response can be seen as a superposition of time-delayed seismic shot records. Using standard shot-record oriented processing and imaging, "crosstalk" between the sources causes the images to be noisy. The crosstalk noise can be reduced by using phase-encoded sources (Bagaini 2006; Ikelle 2007) or simultaneous noise sources (Howe et al. 2007), by randomizing the time interval between the shots (Stefani et al. 2007; Hampson et al. 2008), or by inverting the "blending operator" (Berkhout 2008). Here we briefly discuss deblending as a form of seismic interferometry by MDD.

Consider the configuration depicted in Figure 4, where $\boldsymbol{\sigma}^{(m)}$ denotes a group of source positions $\mathbf{x}_S^{(i)}$. Although the figure suggests that these sources are adjacent to each other, they may also be randomly selected from the total array of sources. Assuming the source at $\mathbf{x}_S^{(i)}$ emits a delayed source wavelet $s^{(i)}(t - t_i)$, the blended inward and outward propagating fields at $\mathbb{S}_{\text{rec}}$ are given by

$$u^{\text{in}}(\mathbf{x}, \boldsymbol{\sigma}^{(m)}, t) = \sum_{\mathbf{x}_S^{(i)} \in \boldsymbol{\sigma}^{(m)}} G^{\text{in}}(\mathbf{x}, \mathbf{x}_S^{(i)}, t) * s^{(i)}(t - t_i),$$

(38)

$$u^{\text{out}}(\mathbf{x}_B, \boldsymbol{\sigma}^{(m)}, t) = \sum_{\mathbf{x}_S^{(i)} \in \boldsymbol{\sigma}^{(m)}} G^{\text{out}}(\mathbf{x}_B, \mathbf{x}_S^{(i)}, t) * s^{(i)}(t - t_i),$$

(39)

where $\mathbf{x}_S^{(i)} \in \boldsymbol{\sigma}^{(m)}$ denotes that the summation takes place over all source positions $\mathbf{x}_S^{(i)}$ in group $\boldsymbol{\sigma}^{(m)}$. By convolving both sides of equation (24) with $s^{(i)}(t - t_i)$ and summing over all sources in $\boldsymbol{\sigma}^{(m)}$ we obtain, analogous to equation (27),

$$u^{\text{out}}(\mathbf{x}_B, \boldsymbol{\sigma}^{(m)}, t) = \int_{\mathbb{S}_{\text{rec}}} \bar{G}_{\text{d}}^{\text{out}}(\mathbf{x}_B, \mathbf{x}, t) * u^{\text{in}}(\mathbf{x}, \boldsymbol{\sigma}^{(m)}, t) \, d\mathbf{x}.$$

(40)

When the indicated receivers on $\mathbb{S}_{\text{rec}}$ are real receivers in a borehole, then $u^{\text{out}}(\mathbf{x}_B, \boldsymbol{\sigma}^{(m)}, t)$ and $u^{\text{in}}(\mathbf{x}, \boldsymbol{\sigma}^{(m)}, t)$ are (decomposed) measured blended wave fields in the borehole. On the other hand, in case of surface data acquisition, $u^{\text{out}}(\mathbf{x}_B, \boldsymbol{\sigma}^{(m)}, t)$ represents the blended data after model-based receiver redatuming to $\mathbb{S}_{\text{rec}}$ and $u^{\text{in}}(\mathbf{x}, \boldsymbol{\sigma}^{(m)}, t)$ represents the blended sources, forward extrapolated through the model to $\mathbb{S}_{\text{rec}}$.

Analogous to section 4.3 we obtain the normal equation by crosscorrelating both sides of equation (40) with $u^{\text{in}}(\mathbf{x}_A, \boldsymbol{\sigma}^{(m)}, t)$ (with $\mathbf{x}_A$ on $\mathbb{S}_{\text{rec}}$) and taking the sum over all source groups $\boldsymbol{\sigma}^{(m)}$. This gives

$$C(\mathbf{x}_B, \mathbf{x}_A, t) = \int_{\mathbb{S}_{\text{rec}}} \bar{G}_{\text{d}}^{\text{out}}(\mathbf{x}_B, \mathbf{x}, t) * \Gamma(\mathbf{x}, \mathbf{x}_A, t) \, d\mathbf{x}, \quad (41)$$
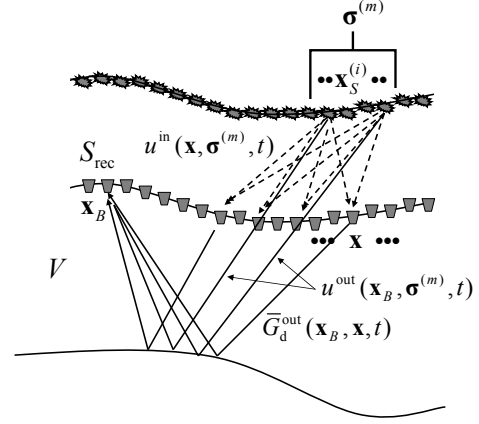

Figure 4. *Convolutional model underlying deblending by MDD.*

where

$$C(\mathbf{x}_B, \mathbf{x}_A, t)$$
$$= \sum_m u^{\text{out}}(\mathbf{x}_B, \boldsymbol{\sigma}^{(m)}, t) * u^{\text{in}}(\mathbf{x}_A, \boldsymbol{\sigma}^{(m)}, -t),$$

(42)

$$\Gamma(\mathbf{x}, \mathbf{x}_A, t)$$
$$= \sum_m u^{\text{in}}(\mathbf{x}, \boldsymbol{\sigma}^{(m)}, t) * u^{\text{in}}(\mathbf{x}_A, \boldsymbol{\sigma}^{(m)}, -t).$$

(43)

The correlation function defined in equation (42) is similar to that in equation (29), except that it is contaminated by crosstalk between the sources within each source group $\boldsymbol{\sigma}^{(m)}$. The point-spread function defined in equation (43) also contains crosstalk contributions. In section 5.1 we present some examples of this point-spread function. Deblending involves inverting equation (41) by MDD. Ideally this eliminates the crosstalk from the correlation function and gives the deblended virtual source response $\bar{G}_{\text{d}}^{\text{out}}(\mathbf{x}_B, \mathbf{x}, t)$.

The discussed deblending process has two interesting limiting cases. When each source group $\boldsymbol{\sigma}^{(m)}$ consists of a single source, the we obtain the expressions for transient sources discussed in sections 4.2 and 4.3. On the other hand, when there is only one source group containing all sources and when the source wavelets are replaced by mutually uncorrelated noise signals, then we obtain the expressions for noise sources discussed in section 4.4.

4.6 Resolving the Green's function

Interferometry by MDD essentially involves inversion of equation (28) (or 41). ~~We formally define the inverse of the point-spread function $\Gamma(\mathbf{x}, \mathbf{x}_A, t)$ as $\Gamma^{\text{inv}}(\mathbf{x}_A, \mathbf{x}', t)$, obeying the relation~~

~~$$\delta(\mathbf{x} - \mathbf{x}')\delta(t) = \int_{\mathbb{S}_{\text{rec}}} \Gamma(\mathbf{x}, \mathbf{x}_A, t) * \Gamma^{\text{inv}}(\mathbf{x}_A, \mathbf{x}', t) \, d\mathbf{x}_A,$$~~

~~where $\delta(\mathbf{x} - \mathbf{x}')$ is defined for $\mathbf{x}$ and $\mathbf{x}'$ both on $\mathbb{S}_{\text{rec}}$. With this inverse point-spread function, interferometry by MDD~~

is formally described by

$$\bar{G}_{\mathrm{d}}(\mathbf{x}_B,\mathbf{x}',t) = \int_{\mathbb{S}_{\mathrm{rec}}} C(\mathbf{x}_B,\mathbf{x}_A,t) * \Gamma^{\mathrm{inv}}(\mathbf{x}_A,\mathbf{x}',t)\,\mathrm{d}\mathbf{x}_A.$$

In general, the existence of the inverse of the point-spread function $\Gamma^{\mathrm{inv}}(\mathbf{x}_A,\mathbf{x}',t)$ is not guaranteed. Recall from equations (30), (33) and (43) that the point-spread function (explicitly or implicitly) involves a summation over source positions. according to $\sum_i u^{\mathrm{in}}(\mathbf{x},\mathbf{x}_S^{(i)},t) * u^{\mathrm{in}}(\mathbf{x}_A,\mathbf{x}_S^{(i)},t)$. To compute this function, the source positions do not need to be known and the source distribution does not need to be regular, but clearly the well-posedness of its inverse depends on the number of available sources, the total source aperture and the source bandwidth. In practical situations a spectral analysis of the point-spread function helps to assess for which spatial and temporal frequencies the inversion can be carried out (van der Neut et al. 2011). The delta functions on the left-hand side of equation (xx) will always be approximated by band-limited functions.

For the actual inversion of equation (28) (or 41) we transform this equation to the frequency domain and replace the integration along the receivers by a summation, according to

$$\hat{C}(\mathbf{x}_B,\mathbf{x}_A^{(l)},\omega) = \sum_k \hat{\bar{G}}_{\mathrm{d}}(\mathbf{x}_B,\mathbf{x}^{(k)},\omega)\hat{\Gamma}(\mathbf{x}^{(k)},\mathbf{x}_A^{(l)},\omega), \quad (44)$$

for all $\mathbf{x}_A^{(l)}$ on the receiver surface $\mathbb{S}_{\mathrm{rec}}$. Note that this discretization assumes a regular sampling of the receiver coordinate $\mathbf{x}^{(k)}$. This is not a severe restriction a less severe restriction than that for discretizing a source integral (like the one in equation (11)), because the receivers are usually often well sampled and their positions are usually known. In case of irregular receiver sampling, a regularization procedure (Duijndam et al. 1999) could be applied prior to inverting equation (44). The system of equations (44) can be solved for $\hat{\bar{G}}_{\mathrm{d}}(\mathbf{x}_B,\mathbf{x}^{(k)},\omega)$ for each frequency component separately. In practice this is done by a stabilized matrix inversion per frequency component, while taking care of the limitations discussed above. Transforming the end-result back to the time domain gives a band-limited estimate of $\bar{G}_{\mathrm{d}}(\mathbf{x}_B,\mathbf{x}^{(k)},t)$, which completes the MDD process.

It is beyond the scope of this paper to discuss the numerical aspects of the matrix inversion. The inversion is similar to that proposed by Berkhout (1982) and Wapenaar & Berkhout (1989) in the context of inverse seismic wavefield extrapolation and imaging. Tanter et al. (2000) apply matrix inversion to a measured wave-field propagator in the context of the time-reversal method and thus improve the source imaging capabilities of that method. Whereas Berkhout (1982) proposes least-squares inversion, Tanter et al. (2000) employ singular-value decomposition to invert the matrix. Similarly, in seismic interferometry by MDD the matrix inversion can be done by least-squares inversion (Wapenaar et al. 2008b) or by singular-value decomposition (Minato et al. 2011). We refer to van der Neut et al. (2011) for a discussion on the stability aspects of interferometry by MDD, and to Ruigrok et al. (2010) and Hunziker et al. (2011) for a discussion on the sampling and illumination aspects.

Within the spectral band for which the point-spread function is invertible, the MDD approach compensates for differences in the source types, variations of the autocorre-

lation functions, nonuniform radiation characteristics and even spatially extended sources (e.g. plane-wave sources with different directions, as in teleseismic data) because all these effects are accounted for in the underlying equations (27) and (40). The application inversion of equation (28) (or 41) requires that data are acquired on a regular (or regularizable) receiver array. Moreover, for the application of equations (29), (30), (32), (33), (42) and (43) it is required that the inward propagating field can be separated from the total field in one way or another. The latter aspect will be discussed on a case-by-case basis in the example sections.

Interferometry by MDD is from a theoretical point of view more accurate than the crosscorrelation approach but the involved processing is less attractive because it is not a trace-by-trace process but involves the inversion of a large system of equations. In sections 5 and 6 we discuss several applications and demonstrate that MDD has the potential to improve the radiation pattern of the virtual source, account for crosstalk of simultaneous source acquisition, suppress multiples, account for dissipation and correct for an irregular source distribution.

4.7 Vectorial fields

Until now we considered scalar fields. For vectorial fields the representations and algorithms are straightforward extensions of those discussed above. Here we discuss the main modifications. The convolutional representation (27) is for vectorial fields extended to

$$\mathbf{u}(\mathbf{x}_B,\mathbf{x}_S^{(i)},t) = \int_{\mathbb{S}_{\mathrm{rec}}} \bar{\mathbf{G}}_{\mathrm{d}}(\mathbf{x}_B,\mathbf{x},t) * \mathbf{u}^{\mathrm{in}}(\mathbf{x},\mathbf{x}_S^{(i)},t)\,\mathrm{d}\mathbf{x} \qquad (45)$$

(the integrand is a convolutional matrix-vector product). Here $\mathbf{u}^{\mathrm{in}}(\mathbf{x},\mathbf{x}_S^{(i)},t)$ and $\mathbf{u}(\mathbf{x}_B,\mathbf{x}_S^{(i)},t)$ are the inward propagating and total (or outward propagating) field vectors, respectively, due to transient sources at $\mathbf{x}_S^{(i)}$ (in the case of simultaneous source acquisition, the source positions $\mathbf{x}_S^{(i)}$ need to be replaced by source groups $\boldsymbol{\sigma}^{(m)}$). For example, for the situation of elastodynamic waves these the field vectors are defined as

$$\mathbf{u}^{\mathrm{in}} = \begin{pmatrix} \Phi^{\mathrm{in}} \\ \Psi^{\mathrm{in}} \\ \Upsilon^{\mathrm{in}} \end{pmatrix} \quad \text{and} \quad \mathbf{u} = \begin{pmatrix} \Phi \\ \Psi \\ \Upsilon \end{pmatrix}, \qquad (46)$$

where Φ, Ψ and Υ represent P, S_1 and S_2 waves, respectively. In practice these fields are obtained by applying decomposition of multi-component data. Moreover, for this situation, $\bar{\mathbf{G}}_{\mathrm{d}}(\mathbf{x}_B,\mathbf{x},t)$ can be written as

$$\bar{\mathbf{G}}_{\mathrm{d}}(\mathbf{x}_B,\mathbf{x},t) = \begin{pmatrix} \bar{G}_{\mathrm{d}}^{\phi,\phi} & \bar{G}_{\mathrm{d}}^{\phi,\psi} & \bar{G}_{\mathrm{d}}^{\phi,v} \\ \bar{G}_{\mathrm{d}}^{\psi,\phi} & \bar{G}_{\mathrm{d}}^{\psi,\psi} & \bar{G}_{\mathrm{d}}^{\psi,v} \\ \bar{G}_{\mathrm{d}}^{v,\phi} & \bar{G}_{\mathrm{d}}^{v,\psi} & \bar{G}_{\mathrm{d}}^{v,v} \end{pmatrix}(\mathbf{x}_B,\mathbf{x},t), \quad (47)$$

where the Green's function $\bar{G}_{\mathrm{d}}^{p,q}(\mathbf{x}_B,\mathbf{x},t)$ is the dipole response (analogous to equation (21)) of the medium in $\mathbb{V}$ (with absorbing boundary conditions at $\mathbb{S}_{\mathrm{rec}}$) in terms of an inward propagating q-type wave field at source position $\mathbf{x}$ and a total (or outward propagating) p-type wave field at receiver position $\mathbf{x}_B$ (Wapenaar & Berkhout 1989). When the sources at $\mathbf{x}_S^{(i)}$ are multi-component sources, equation (45) can be extended to

$$\mathbf{U}(\mathbf{x}_B,\mathbf{x}_S^{(i)},t) = \int_{\mathbb{S}_{\mathrm{rec}}} \bar{\mathbf{G}}_{\mathrm{d}}(\mathbf{x}_B,\mathbf{x},t) * \mathbf{U}^{\mathrm{in}}(\mathbf{x},\mathbf{x}_S^{(i)},t)\,\mathrm{d}\mathbf{x}, \quad (48)$$

where $\mathbf{U}^{\mathrm{in}}$ and $\mathbf{U}$ are matrices of which the columns contain field vectors $\mathbf{u}^{\mathrm{in}}$ and $\mathbf{u}$ for different source components (similar as the different columns of $\bar{\mathbf{G}}_{\mathrm{d}}$ are related to different source types). Equations (45) and (48) are not restricted to the elastodynamic situation but apply to any vectorial wave or diffusion field, including electromagnetic, poroelastic and seismoelectric fields (Wapenaar et al. 2008a).

Interferometry by MDD means that equation (48) needs to be solved for $\bar{\mathbf{G}}_{\mathrm{d}}(\mathbf{x}_B, \mathbf{x}, t)$. Similar as for the scalar situation, the well-posedness of this inverse problem depends on the number of available sources, the source aperture, the bandwidth, and, in addition, the number of independent source components. Since the Green's matrix is resolved by MDD, the sources do not need to be regularly distributed and the source components do not need to be mutually orthonormal.

Similar as in the scalar case, to obtain the normal equation for least-squares inversion, we crosscorrelate both sides of equation (48) with the transposed of $\mathbf{U}^{\mathrm{in}}(\mathbf{x}_A, \mathbf{x}_S^{(i)}, t)$ (with $\mathbf{x}_A$ on $\mathbb{S}_{\mathrm{rec}}$) and take the sum over all sources, according to

$$\mathbf{C}(\mathbf{x}_B, \mathbf{x}_A, t) = \int_{\mathbb{S}_{\mathrm{rec}}} \bar{\mathbf{G}}_{\mathrm{d}}(\mathbf{x}_B, \mathbf{x}, t) * \mathbf{\Gamma}(\mathbf{x}, \mathbf{x}_A, t) \, \mathrm{d}\mathbf{x}, \quad (49)$$

where

$$\mathbf{C}(\mathbf{x}_B, \mathbf{x}_A, t) = \sum_i \mathbf{U}(\mathbf{x}_B, \mathbf{x}_S^{(i)}, t) * \{\mathbf{U}^{\mathrm{in}}(\mathbf{x}_A, \mathbf{x}_S^{(i)}, -t)\}^t, \ (50)$$

$$\mathbf{\Gamma}(\mathbf{x}, \mathbf{x}_A, t) = \sum_i \mathbf{U}^{\mathrm{in}}(\mathbf{x}, \mathbf{x}_S^{(i)}, t) * \{\mathbf{U}^{\mathrm{in}}(\mathbf{x}_A, \mathbf{x}_S^{(i)}, -t)\}^t, \quad (51)$$

with superscript ^{t} denoting transposition. Here $\mathbf{C}(\mathbf{x}_B, \mathbf{x}_A, t)$ and $\mathbf{\Gamma}(\mathbf{x}, \mathbf{x}_A, t)$ are the correlation and point-spread functions, respectively, in matrix form. Equation (49) shows again that the correlation function is proportional to the sought Green's function $\bar{\mathbf{G}}_{\mathrm{d}}(\mathbf{x}_B, \mathbf{x}, t)$ with its source smeared in space and time by the point-spread function.

For the situation of noise sources the correlation and point-spread matrices are given by

$$\mathbf{C}(\mathbf{x}_B, \mathbf{x}_A, t) = \langle \mathbf{u}(\mathbf{x}_B, t) * \{\mathbf{u}^{\mathrm{in}}(\mathbf{x}_A, -t)\}^t \rangle, \quad (52)$$

$$\mathbf{\Gamma}(\mathbf{x}, \mathbf{x}_A, t) = \langle \mathbf{u}^{\mathrm{in}}(\mathbf{x}, t) * \{\mathbf{u}^{\mathrm{in}}(\mathbf{x}_A, -t)\}^t \rangle, \quad (53)$$

where, analogous to equations $(34) - (36)$, the field vectors $\mathbf{u}^{\mathrm{in}}$ and $\mathbf{u}$ are the responses of simultaneously acting mutually uncorrelated multi-component noise sources. It can be shown in a similar way as in section 4.4 that the correlation and point-spread functions defined in equations (52) and (53) are identical to those defined in (50) and (51). Hence, whether we consider transient or noise sources, equation (49) is the relation that needs to be inverted by MDD to resolve the Green's function $\bar{\mathbf{G}}_{\mathrm{d}}(\mathbf{x}_B, \mathbf{x}, t)$. This is done in a similar way as described in section 4.6 for the scalar situation.

5 APPLICATIONS IN CONTROLLED-SOURCE INTERFEROMETRY

Unlike ambient-noise interferometry, controlled-source interferometry is usually applied to situations in which the sources are regularly distributed along a surface (Schuster 2009). Hence, for controlled-source interferometry, MDD is usually not required to correct for an irregular source distribution. However, there are several other limiting factors in

controlled-source interferometry for which MDD may provide a solution. In the following sections we show with numerical examples how MDD accounts for the effects of medium inhomogeneities in the "virtual source method" (section 5.1), for multiples in the illuminating wave field in ocean-bottom multiple elimination (section 5.2) and for losses in CSEM interferometry (section 5.3).

5.1 "Virtual source method"

Although creating a virtual source is the essence of all seismic interferometry methods, in the seismic exploration literature the term "virtual source method" is often synonymous with the method developed by Bakulin & Calvert (2004, 2006). Figure 2b shows the basic configuration. Sources are present at the Earth's surface, denoted by $\mathbb{S}_{\mathrm{src}}$. The responses of these sources are measured in a near-horizontal borehole, below a complex overburden. The responses $u(\mathbf{x}_A, \mathbf{x}_S, t)$ and $u(\mathbf{x}_B, \mathbf{x}_S, t)$ at any combination of two receivers $\mathbf{x}_A$ and $\mathbf{x}_B$ in the borehole are crosscorrelated and the results are integrated along the sources $\mathbf{x}_S$ at $\mathbb{S}_{\mathrm{src}}$, according to equation (11). The correlation function $C(\mathbf{x}_B, \mathbf{x}_A, t)$ is interpreted as the response at $\mathbf{x}_B$ of a virtual source at $\mathbf{x}_A$. Because this virtual source is situated below the complex overburden, its response contains less-distorted reflections of the deeper target than the original response of the source at the surface $\mathbb{S}_{\mathrm{src}}$.

From the theory it follows that this method involves approximations. If $\mathbb{S}_{\mathrm{src}}$ were a closed surface, the correlation function $C(\mathbf{x}_B, \mathbf{x}_A, t)$ would be proportional to $\{G(\mathbf{x}_B, \mathbf{x}_A, t) + G(\mathbf{x}_B, \mathbf{x}_A, -t)\} * S(t)$ (equation 13), in which $G(\mathbf{x}_B, \mathbf{x}_A, t) * S(t)$ is indeed the response of a virtual source at $\mathbf{x}_A$. However, because $\mathbb{S}_{\mathrm{src}}$ is limited to a part of the Earth's surface, the correlation function is a distorted version of $G(\mathbf{x}_B, \mathbf{x}_A, t) * S(t)$ and contains spurious multiples (Snieder et al. 2006b). To compensate for this, Bakulin & Calvert (2004) apply a time window around the first arrival of $u(\mathbf{x}_A, \mathbf{x}_S, t)$. Bakulin & Calvert (2006) propose to replace the correlation of $u(\mathbf{x}_B, \mathbf{x}_S, t)$ with $u(\mathbf{x}_A, \mathbf{x}_S, t)$ by a trace-by-trace deconvolution for the downgoing part of $u(\mathbf{x}_A, \mathbf{x}_S, t)$. They show that this approach compensates for variations in the source wavelet and, partly, for reverberations in the overburden. The spurious multiples can be further suppressed by applying up/down decomposition to $u(\mathbf{x}_B, \mathbf{x}_S, t)$ as well as $u(\mathbf{x}_A, \mathbf{x}_S, t)$ (Mehta et al. 2007a; van der Neut & Wapenaar 2009).

We illustrate the correlation approach with a numerical example. Figure 5a shows the configuration, with a regular distribution of sources at the surface (denoted by the black dots) and receivers in a horizontal borehole (the green triangles at $x_3 = 500$ m). The upper part of the overburden, i.e., the medium between the sources and the receivers, contains significant variations of the medium parameters in the lateral as well as in the vertical direction. Below the receivers there is a reservoir layer (the orange layer in Figure 5a). The lower part of the overburden, i.e., the medium between the receivers in the borehole and the reservoir, is homogeneous (the light-green layer). Figure 5b shows a modeled response of a source at the center of the surface, observed by the receivers in the borehole. The modeling was done without free-surface effects. The response of the reservoir is denoted by the arrow. Note that it is distorted by the inhomogeneities
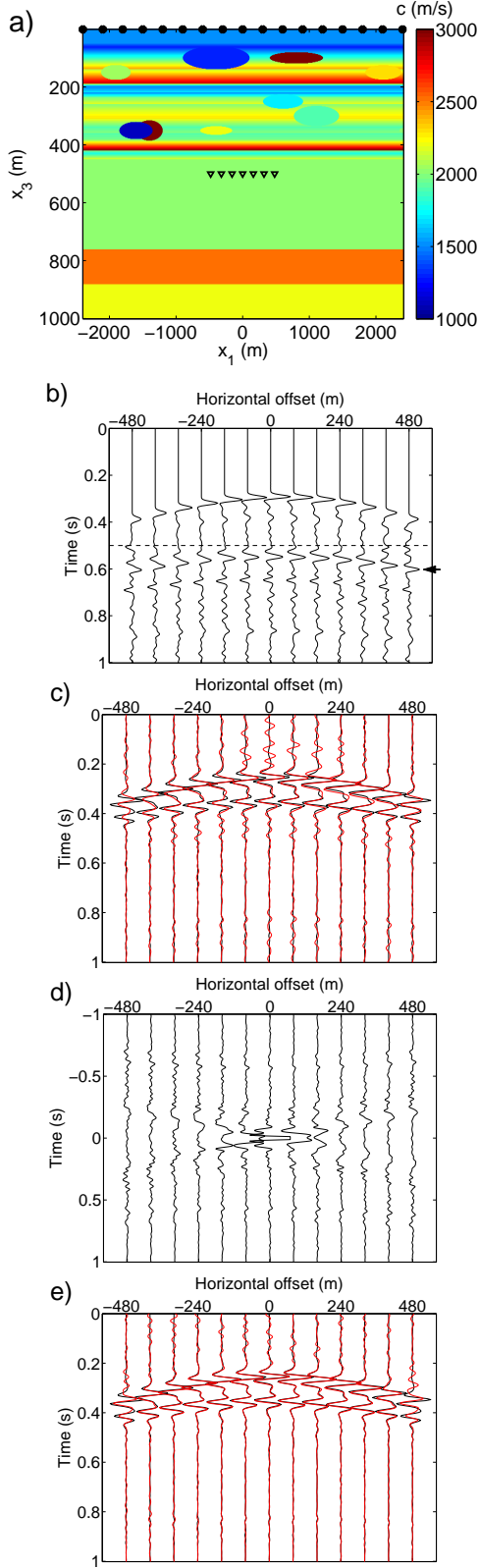
Figure 5. *(a) Configuration for the "virtual source method". The sources are situated at the surface (black dots) and the receivers in a horizontal borehole (the green triangles at $x_3 = 500m$), below a complex overburden. (b) Modeled response of a source at the center of the surface. The amplitudes below the dashed line have been multiplied by a factor 3. (c) Result of interferometry by crosscorrelation of decomposed wave fields (red) compared with directly modeled reflection response of a source at the center of the borehole (black). (d) Point-spread function (clipped at 20% of its maximum amplitude). (e) MDD result (red) compared with modeled response (black).*

of the overburden. The aim of the "virtual source method" is to reduce these distortions. We follow the approach of Mehta et al. (2007a), hence, we first apply decomposition of the field observed in the borehole into downgoing and upgoing waves. This requires that multi-component data are available (in this case the acoustic pressure and the normal particle velocity component). We call the decomposed fields $u^{\text{in}}(\mathbf{x}_A, \mathbf{x}_S^{(i)}, t)$ and $u^{\text{out}}(\mathbf{x}_B, \mathbf{x}_S^{(i)}, t)$, respectively. The correlation function is defined, analogous to equation (29), as

$$C(\mathbf{x}_B, \mathbf{x}_A, t) = \sum_i u^{\text{out}}(\mathbf{x}_B, \mathbf{x}_S^{(i)}, t) * u^{\text{in}}(\mathbf{x}_A, \mathbf{x}_S^{(i)}, -t). \quad (54)$$

Figure 5c shows this correlation function in red. The virtual source at $\mathbf{x}_A$ is chosen at the center of the borehole whereas the receiver coordinate $\mathbf{x}_B$ varies along the borehole. The directly modeled reflection response of a source for downgoing waves at $\mathbf{x}_A$ is shown in black in this same figure. Note that the retrieved reservoir response ~~shows less distortions than the original response in Figure 5b. It~~ matches the modeled response reasonably well, but still we observe some distortions along this reflection event as well as some spurious events at later times.

Interferometry by MDD provides a more accurate way to retrieve the virtual source response. Figure 3b shows the configuration. Assuming a regular source distribution, this configuration corresponds to that of Figure 2b, except that Figure 3b illustrates the convolutional representation that underlies MDD. The response $u^{\text{out}}(\mathbf{x}_B, \mathbf{x}_S^{(i)}, t)$ is defined, analogous to equation (27), as

$$u^{\text{out}}(\mathbf{x}_B, \mathbf{x}_S^{(i)}, t) = \int_{\mathbb{S}_{\text{rec}}} \bar{G}_{\text{d}}^{\text{out}}(\mathbf{x}_B, \mathbf{x}, t) * u^{\text{in}}(\mathbf{x}, \mathbf{x}_S^{(i)}, t) \, d\mathbf{x}, \quad (55)$$

i.e., the convolution of the inward propagating wave field $u^{\text{in}}(\mathbf{x}, \mathbf{x}_S^{(i)}, t)$ with the Green's function $\bar{G}_{\text{d}}^{\text{out}}(\mathbf{x}_B, \mathbf{x}, t)$, integrated along the receivers $\mathbf{x}$ in the borehole. This borehole is denoted as $\mathbb{S}_{\text{rec}}$. Our aim is to retrieve $\bar{G}_{\text{d}}^{\text{out}}(\mathbf{x}_B, \mathbf{x}, t)$ by inverting, analogous to equation (28),

$$C(\mathbf{x}_B, \mathbf{x}_A, t) = \int_{\mathbb{S}_{\text{rec}}} \bar{G}_{\text{d}}^{\text{out}}(\mathbf{x}_B, \mathbf{x}, t) * \Gamma(\mathbf{x}, \mathbf{x}_A, t) \, d\mathbf{x}. \quad (56)$$

The correlation function $C(\mathbf{x}_B, \mathbf{x}_A, t)$ at the left-hand side was already shown in Figure 5c. The point-spread function $\Gamma(\mathbf{x}, \mathbf{x}_A, t)$ at the right-hand side is obtained, according to equation (30), by crosscorrelating $u^{\text{in}}(\mathbf{x}, \mathbf{x}_S^{(i)}, t)$ with $u^{\text{in}}(\mathbf{x}_A, \mathbf{x}_S^{(i)}, t)$ and summing over the sources. It is shown in Figure 5d for fixed $\mathbf{x}_A$ and variable $\mathbf{x}$. Note that it deviates significantly from ~~a delta function in space and time~~ the band-limited delta function in Figure A1, due to the inhomogeneities of the overburden. According to equation (56) this point-spread function smears the source of $\bar{G}_{\text{d}}^{\text{out}}(\mathbf{x}_B, \mathbf{x}, t)$ in space and time, which explains the distortions along the reflection event in Figure 5c. By applying MDD, that is, deconvolving the correlation function in Figure 5c for the point-spread function of Figure 5d, we obtain an estimate of the Green's function $\bar{G}_{\text{d}}^{\text{out}}(\mathbf{x}_B, \mathbf{x}, t)$. The result (for $\mathbf{x} = \mathbf{x}_A$ fixed at the central geophone and variable $\mathbf{x}_B$) is shown in Figure 5e by the red traces (for display purposes convolved with $S(t)$), where it is compared with the directly modeled response (black traces). Note that the match is nearly perfect and that the spurious events vanished, which confirms that in this example MDD properly corrects for the inhomogeneities of the overburden.

The elastodynamic extension of this approach yields improved virtual P- and S-wave source responses with reliable amplitudes along the reflection events (van der Neut et al. 2011), suited for quantitative amplitude-versus-offset (AVO) inversion. A further discussion is beyond the scope of this paper.

We conclude this section by presenting the point-spread function for the situation of simultaneous source acquisition. We consider a similar configuration as in Figure 5a, except that for simplicity the propagation velocity is taken constant at 2000 m/s. There are 256 sources at the surface with a lateral spacing of 20 m. We form 64 source groups $\boldsymbol{\sigma}^{(m)}$, each containing four adjacent sources which emit transient wavelets, 0.25 s after one another. The inward propagating field $u^{\mathrm{in}}(\mathbf{x}, \boldsymbol{\sigma}^{(m)}, t)$ at the receiver array at $x_3 = 500$ m is defined by equation (38). The point-spread function $\Gamma(\mathbf{x}, \mathbf{x}_A, t)$, as defined in equation (43), is shown in Figure 6a,* with $\mathbf{x}_A$ fixed at the center of the array and $\mathbf{x}$ variable along the array. Note that the band-limited delta function around $\mathbf{x} = \mathbf{x}_A$ and $t = 0$ resembles that in Figure A1 because the medium is homogeneous in both cases. However, Figure 6a contains in addition a number of temporally and spatially shifted band-limited delta functions, as a result of the crosstalk between the sources within each source group $\boldsymbol{\sigma}^{(m)}$. These shifted delta functions account for the crosstalk in the correlation function $C(\mathbf{x}_B, \mathbf{x}_A, t)$ via equation (41). To obtain the deblended virtual source response $\bar{G}_{\mathrm{d}}^{\mathrm{out}}(\mathbf{x}_B, \mathbf{x}, t)$ from $C(\mathbf{x}_B, \mathbf{x}_A, t)$, equation (41) needs to be inverted.

As mentioned in section 4.5, the crosstalk noise associated to standard shot-record oriented processing of blended data is sometimes reduced by randomizing the time interval between the shots. We add random variations (uniform between $+$ and -50%) to the 0.25 s time interval and evaluate again the point-spread function $\Gamma(\mathbf{x}, \mathbf{x}_A, t)$, see Figure 6b. Note that the band-limited delta function around $\mathbf{x} = \mathbf{x}_A$ and $t = 0$ remains intact, whereas the crosstalk disperses in space and time. Inverting noisy point-spread functions like the one in Figure 6b may be a more stable process than inverting nearly periodic point-spread functions like the one in Figure 6a.

5.2 Ocean-bottom multiple elimination

As already mentioned in the introduction, interferometry by MDD is akin to multiple elimination of ocean-bottom data (Wapenaar et al. 2000; Amundsen 2001). Here we briefly review ocean-bottom multiple elimination, explained as an interferometry-by-MDD process. Figure 7 shows the convolutional model of Figure 3b, modified for the situation of ocean-bottom data, including multiple reflections. Equation (55) gives the relation between the inward and outward propagating fields at the ocean bottom and the Green's function $\bar{G}_{\mathrm{d}}^{\mathrm{out}}(\mathbf{x}_B, \mathbf{x}, t)$. Recall that the bar denotes a reference situation with possibly different boundary conditions at $\mathbb{S}_{\mathrm{rec}}$ and/or different medium parameters outside $\mathbb{V}$. For the reference situation we choose an absorbing ocean bottom $\mathbb{S}_{\mathrm{rec}}$ and a homogeneous upper half-space, which implies that $\bar{G}_{\mathrm{d}}^{\mathrm{out}}(\mathbf{x}_B, \mathbf{x}, t)$ is the response of the half-space below $\mathbb{S}_{\mathrm{rec}}$,
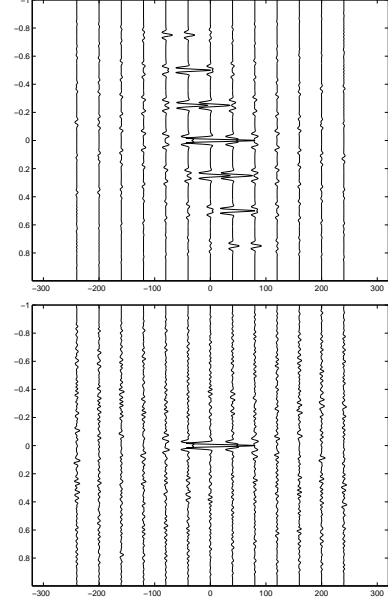

Figure 6. *(a) Point-spread function (clipped at 20% of its maximum amplitude) for blended data from 64 groups of four sources each, with a regular time interval of 0.25 s. (b) Idem, after adding random variations to the time interval.*

without any multiple reflections related to the ocean bottom and the water surface. Interferometry by MDD involves resolving $\bar{G}_{\mathrm{d}}^{\mathrm{out}}(\mathbf{x}_B, \mathbf{x}, t)$ by inverting equation (56).

We illustrate this with a numerical example. Figure 8a shows the configuration, with sources at the water surface and multi-component receivers (acoustic pressure and normal particle velocity) at the ocean bottom. The lower half-space contains a reservoir layer. Figure 8b shows the modeled response of the central source, observed at the ocean bottom. The direct wave and the reservoir response (the latter denoted by an arrow) are clearly distinguishable, as well as many multiple reflections. Decomposition is applied to the multi-component data at the ocean bottom, using the medium parameters of the first layer below the ocean bottom (Amundsen & Reitan 1995; Schalkwijk et al. 2003). This gives the inward and outward propagating waves $u^{\mathrm{in}}(\mathbf{x}_A, \mathbf{x}_S^{(i)}, t)$ and $u^{\mathrm{out}}(\mathbf{x}_B, \mathbf{x}_S^{(i)}, t)$ just below the ocean bottom. The correlation function, defined in equation (54), is shown in Figure 8c (red traces), and is compared with the di-
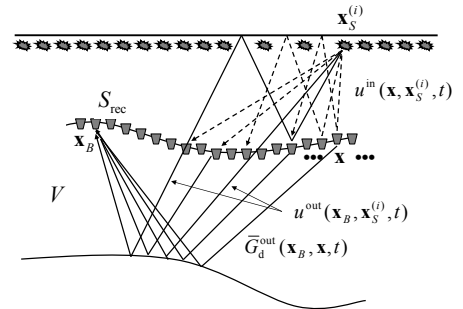

Figure 7. *Convolutional model for ocean-bottom data with multiples.*

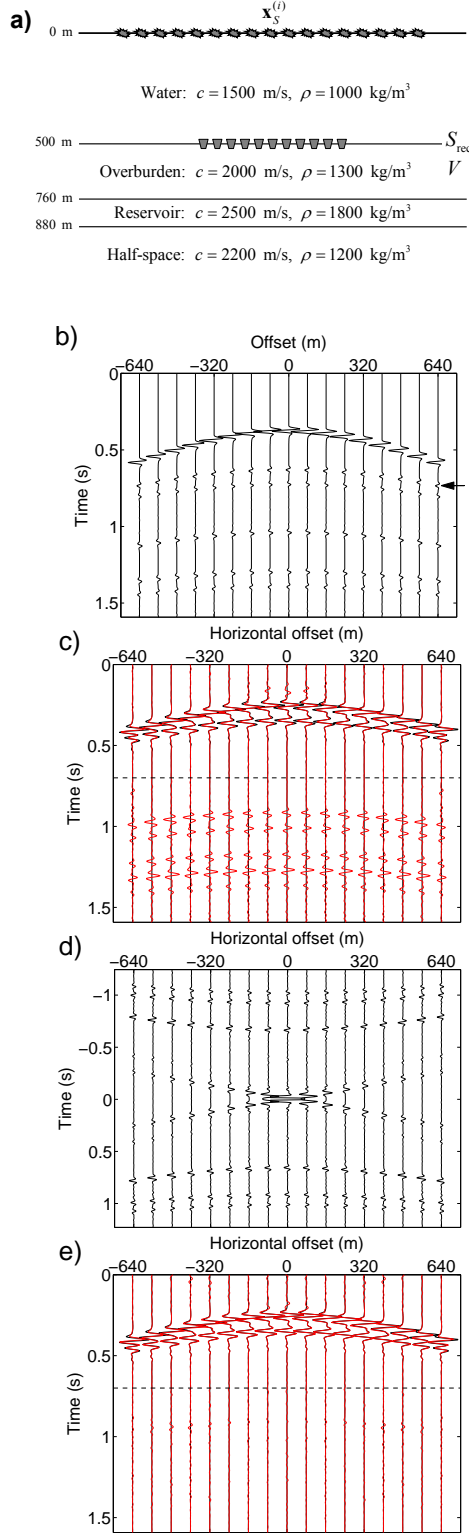* Layout (including clip-factor) to be modified.

Figure 8. *(a) Configuration for ocean-bottom multiple elimination. The sources are situated just below the free surface and the receivers at the ocean bottom. (b) Modeled response of a source at the center of the surface. (c) Result of interferometry by cross-correlation of decomposed wave fields (red) compared with directly modeled reflection response of a source at the center of the ocean bottom (black). The amplitudes below the dashed line have been multiplied by a factor 3. (d) Point-spread function (clipped at 20% of its maximum amplitude). (e) MDD result (red) compared with modeled response (black). The amplitudes below the dashed line have been multiplied by a factor 3.*

rectly modeled response of the reservoir layer (black traces). Note that the match of the correlation function with the reservoir response is quite good, but the correlation function contains in addition many spurious multiple reflections that are not present in the reservoir response. The amplitudes of these spurious multiple reflections, which appear below the horizontal dashed line in Figure 8c, have been multiplied by a factor three for display purposes (in more complicated situations these spurious multiples would interfere with the retrieved primaries). The point-spread function $\Gamma(\mathbf{x}, \mathbf{x}_A, t)$, defined in equation (30), is shown in Figure 8d. Apart from the ~~smeared~~ band-limited delta function, it contains multiple reflections. According to equation (56), the correlation function in Figure 8c can be seen as the reservoir response $\bar{G}_{\mathrm{d}}^{\mathrm{out}}(\mathbf{x}_B, \mathbf{x}, t)$ ~~of which the source is~~ convolved in space and time with the point-spread function in Figure 8d. This explains the spurious multiples in Figure 8c. These spurious multiples are removed by deconvolving for the point-spread function, i.e., by inverting equation (56) for $\bar{G}_{\mathrm{d}}^{\mathrm{out}}(\mathbf{x}_B, \mathbf{x}, t)$. The result of this MDD procedure (for $\mathbf{x} = \mathbf{x}_A$ fixed at the central geophone and variable $\mathbf{x}_B$) is shown in Figure 8e by the red traces (for display purposes convolved with $S(t)$), compared with the directly modeled response (black traces). Note that the spurious multiples of Figure 8c have been very well suppressed (for display purposes the amplitudes of the multiple residuals below the dashed line in Figure 8e have been multiplied with the same factor as the spurious multiples in Figure 8c).

We included this example to show the relation between interferometry by MDD and the methodology of ocean-bottom multiple elimination. In the example in section 5.1 we showed that interferometry by MDD accounts for overburden distortions, but in that example the effect of multiple reflections was small. When borehole data are distorted by overburden effects as well as multiple reflections, interferometry by MDD simultaneously accounts for both types of distortions.

5.3 CSEM interferometry

In controlled-source electromagnetic (CSEM) prospecting, a low-frequency source above the ocean bottom emits a diffusive EM field into the subsurface, of which the response is measured by multi-component EM receivers at the ocean bottom (Figure 9a). Although the spatial resolution of CSEM data is much lower than that of seismic data, an important advantage of CSEM prospecting is its potential to detect a hydrocarbon accumulation in a reservoir due to its high conductivity contrast (Ellingsrud et al. 2002; Moser et al. 2006). Figure 9b shows a modeled 2D CSEM response of an inline electric current source of 0.5 Hz. The source is positioned at the center of the array, 50 m above the ocean bottom, see Figure 9a. This response represents the inline electric field component at the ocean bottom, as a function of source-receiver offset. The receiver sampling is 20 m and the total length of the array is 10 km.

Because a CSEM measurement is nearly monochromatic, the response of a reservoir cannot be separated in time from other events. As a matter of fact, it is largely overshadowed by the direct field and the response of the airwave. Amundsen et al. (2006) show that decomposition of CSEM data into downward and upward decaying fields
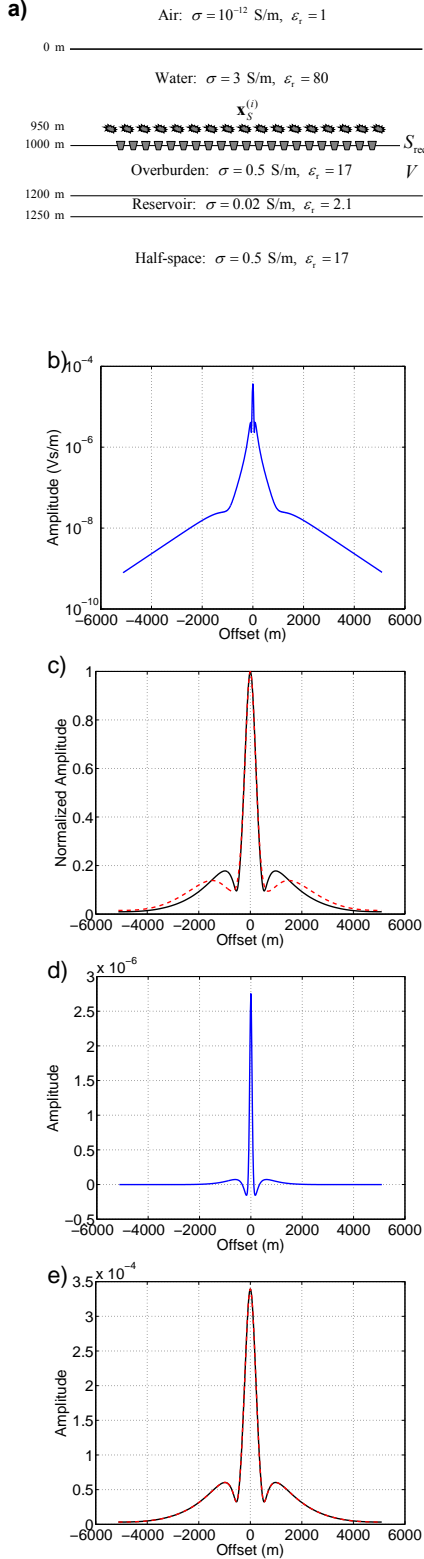
improves the detectability of hydrocarbon reservoirs. Here we show that the combination of decomposition and interferometry by MDD yields accurate quantitative information about the reservoir response (Slob et al. 2007; van den Berg et al. 2008).

Decomposition requires that multi-component data are available. For the example of Figure 9, this means that apart from the inline electric field data (Figure 9b), transverse magnetic data are required as well. Using a decomposition algorithm similar as that for seismic data, CSEM data can be decomposed into downward and upward decaying fields (Ursin 1983; Amundsen et al. 2006). We designate these fields as $\hat{u}^{\text{in}}(\mathbf{x}_A, \mathbf{x}_S^{(i)}, \omega)$ and $\hat{u}^{\text{out}}(\mathbf{x}_B, \mathbf{x}_S^{(i)}, \omega)$, respectively, where superscripts "in" and "out" denote that at the receiver surface $\mathbb{S}_{\text{rec}}$ in Figure 9a these fields diffuse inward to and outward from $\mathbb{V}$, respectively. Note that ω is considered constant ($\omega = 2\pi f$, with $f = 0.5$ Hz).

Because in CSEM we consider monochromatic fields, we replace equations (56), (54) and (30) by the following frequency domain expressions

$$\hat{C}(\mathbf{x}_B, \mathbf{x}_A, \omega) = \int_{\mathbb{S}_{\text{rec}}} \hat{\bar{G}}_{\text{d}}^{\text{out}}(\mathbf{x}_B, \mathbf{x}, \omega)\hat{\Gamma}(\mathbf{x}, \mathbf{x}_A, \omega) \, \text{d}\mathbf{x}, \quad (57)$$

where the correlation function and the point-spread function are defined as

$$\hat{C}(\mathbf{x}_B, \mathbf{x}_A, \omega) = \sum_i \hat{u}^{\text{out}}(\mathbf{x}_B, \mathbf{x}_S^{(i)}, \omega)\{\hat{u}^{\text{in}}(\mathbf{x}_A, \mathbf{x}_S^{(i)}, \omega)\}^*, (58)$$

$$\hat{\Gamma}(\mathbf{x}, \mathbf{x}_A, \omega) = \sum_i \hat{u}^{\text{in}}(\mathbf{x}, \mathbf{x}_S^{(i)}, \omega)\{\hat{u}^{\text{in}}(\mathbf{x}_A, \mathbf{x}_S^{(i)}, \omega)\}^*, \quad (59)$$

respectively. $\hat{\bar{G}}_{\text{d}}^{\text{out}}(\mathbf{x}_B, \mathbf{x}, \omega)$ in equation (57) is the sought reservoir response that would be obtained with a monochromatic source for an inward diffusing field at $\mathbf{x}$ and a receiver for an outward diffusing field at $\mathbf{x}_B$ (both at $\mathbb{S}_{\text{rec}}$), in a configuration with a reflection-free ocean bottom. The monochromatic correlation function defined in equation (58) is obtained by correlating the inward and outward diffusing fields at $\mathbb{S}_{\text{rec}}$. The result is shown in Figure 9c (red curve), where it is compared with the directly modeled response $\hat{\bar{G}}_{\text{d}}^{\text{out}}(\mathbf{x}_B, \mathbf{x}, \omega)$ (black curve), with $\mathbf{x} = \mathbf{x}_A$ at the center of the array at $\mathbb{S}_{\text{rec}}$. The differences are mainly due to the dissipation of the conducting water layer, for which no compensation takes place in the correlation method. For ease of comparison both responses were normalized so that the maxima of both curves are the same. The deviations at intermediate offsets hinder the quantification of the reservoir parameters.

Figure 9d shows the monochromatic point-spread function, defined in equation (59). It deviates from a band-limited spatial delta function due to the dissipation of the water layer as well as the interactions with the water surface. MDD involves inversion of equation (57), i.e., removing the effect of the point-spread function of Figure 9d from the correlation function in Figure 9c. The result is shown in Figure 9e (red curve), where it perfectly matches the directly modeled result (black curve). Note that, unlike in Figure 9c, no normalization was needed here.

This example shows that, at least in principle, interferometry by MDD compensates for dissipation and thus leads to an accurate retrieval of the CSEM reservoir response. The effects of the conducting water layer are completely eliminated, including those of the direct field and the airwave.

Figure 9. *(a) Configuration for CSEM interferometry. The sources just above the ocean bottom are inline electric current sources, emitting monochromatic diffusive EM fields into the subsurface. The receivers at the ocean bottom measure the inline electric field and the transverse magnetic field. (b) Inline electric field at ocean bottom. (c) Result of interferometry by crosscorrelation (red) compared with directly modeled CSEM reservoir response (black). (d) Point-spread function. (e) MDD result (red) compared with modeled response (black).*

The final response is independent of the water depth and contains quantitative information about the reservoir layer. It should be noted that we considered an ideal situation of well-sampled data, measured with high precision and no noise added. For a more detailed discussion of CSEM interferometry by MDD, see Hunziker et al. (2009, 2011) and Fan et al. (2009).

6   APPLICATIONS IN AMBIENT-NOISE INTERFEROMETRY

In ambient-noise interferometry, the sources are unknown and usually irregularly distributed. MDD has the potential to compensate for the source irregularity. We illustrate this aspect with numerical examples for passive direct-wave interferometry (section 6.1) and for passive reflected-wave interferometry (section 6.2).

6.1   Passive direct-wave interferometry

One of the most widely used applications of direct-wave interferometry is the retrieval of seismic surface waves between seismometers from ambient noise (Campillo & Paul 2003; Shapiro & Campillo 2004; Shapiro et al. 2005; Sabra et al. 2005a,b; Larose et al. 2006; Gerstoft et al. 2006; Yao et al. 2006; Bensen et al. 2007, 2008; Yao et al. 2008; Gouédard et al. 2008a,b; Liang & Langston 2008; Ma et al. 2008; Lin et al. 2009; Picozzi et al. 2009). Usually one considers the retrieval of the fundamental mode only. It is well known that in a layered medium, surface waves consist of a fundamental mode and higher-order modes (e.g. Nolet (1975); Gabriels et al. (1987)). Halliday & Curtis (2008) and Kimman & Trampert (2010) carefully analyze interferometry of surface waves with higher-order modes. They show that, when the primary sources are confined to the surface, crosscorrelation gives rise to spurious interferences between higher-order modes and the fundamental mode, whereas the presence of sources at depth, as prescribed by the theory (Wapenaar & Fokkema 2006), enables the correct recovery of all modes independently. In realistic situations the source distribution is mainly confined to the surface, which explains why in the current practice of surface-wave interferometry only the fundamental modes are properly retrieved.

In agreement with the current practice of surface-wave interferometry, in the following numerical example we consider fundamental Rayleigh-wave modes only. These modes can be treated as the solution of a scalar 2D wave equation with the propagation velocity being the dispersive Rayleigh wave velocity of the layered medium. Hence, for interferometry we can make use of the 2D version of the scalar Green's function representations, discussed in the theory sections. The basic configurations for direct-wave interferometry are shown in Figure 2a for the crosscorrelation method, and in Figure 3a for the MDD method. For the current purpose these figures should be seen as plan views.

Consider Figure 10a, which shows a map of the USA, a number of receiver stations of the USArray (green triangles) and a number of sources along the East coast (blue dots), for example representing storm-generated microseisms (Bromirski 2001). Assuming a layered medium, we compute the dispersion curve of the fundamental mode

Figure 10. *Passive surface-wave interferometry. (a) Map of USA, with USArray stations (green triangles) and storm-generated microseisms (blue dots). (b) Rayleigh-wave dispersion curve (fundamental mode), based on the PREM model. (c) Modeled Rayleigh-wave response along South-North array in central USA. (d) Crosscorrelation result (red) compared with directly modeled response (black). The virtual source is indicated by the red dot in (a). The traces correspond to the irregular receiver stations along the East-West array. (e) The point-spread function along the South-North array. (f) MDD result (red) compared with directly modeled response (black).*

of the Rayleigh-wave for the upper 300 km of the PREM model (Dziewonski & Anderson 1981), using the approach described by Wathelet et al. (2004). The dispersion curve is shown in Figure 10b. We define the sources as simultaneously acting uncorrelated noise sources, with a central frequency of 0.04 Hz. Using the computed dispersion curve, we model the surface wave response of the distribution of noise sources at all indicated receivers. Figure 10c shows 1500 s of the response along the indicated South-North array in central USA (the total ~~modeled~~ duration of the modeled noise responses is approximately two days).

Our aim is to turn one of the receivers of the South-North array (the one indicated by the red dot) into a virtual source and to retrieve the response of this virtual source at the somewhat scattered receiver stations along the East-West array. Following the crosscorrelation method we take the noise response at the receiver indicated by the red dot and crosscorrelate it with each of the responses at the receivers of the East-West array (equation (17), with $\mathbf{x}_A$ fixed and $\mathbf{x}_B$ variable). The result is shown in Figure 10d by the red traces. For comparison, the black traces in this figure represent the directly modeled surface wave response of a source at the position of the red dot, using a source function $S(t)$ equal to the average autocorrelation of the noise. Unlike equation (13), of which the left-hand side shows a causal and an acausal response, the crosscorrelation resulted in a causal contribution only. The explanation for this is that the distribution of sources is restricted to the East coast and hence is not enclosing the receivers. Moreover, although the travel times seem to match reasonably well, some of the seismograms show a small travel time error that corresponds to a velocity shift of the order of one percent. This is not small compared to the velocity shifts that are inverted for in surface wave inversion (several percent). There is also a pronounced mismatch between the amplitudes of the red and black waveforms. These travel time and amplitude perturbations are a result of the irregularity of the source distribution.

The mismatch in Figure 10d is quantified by equation (28), which states that the correlation function (the red traces) is proportional to the Green's function with its source smeared in space and time by the point-spread function $\Gamma(\mathbf{x}, \mathbf{x}_A, t)$. According to equation (33), this point spread function is obtained by crosscorrelating the incoming field at $\mathbf{x}$ with that at $\mathbf{x}_A$, with $\mathbf{x}$ and $\mathbf{x}_A$ both on $\mathbb{S}_{\mathrm{rec}}$ (in this case the South-North array). Because in the current example no scattering takes place, the incoming field is equal to the

total field. We crosscorrelate the full response at the receiver indicated by the red dot (fixed $\mathbf{x}_A$) with all other responses along the South-North array (variable $\mathbf{x}$), see Figure 10e. This point-spread function clearly shows that the virtual source is smeared in space and time. Following the MDD procedure discussed in section 4.6 we resolve the Green's function by applying the inverse of the point-spread function to the correlation function. The result is represented by the red traces in Figure 10f (for display purposes convolved with $S(t)$), where it is compared again with the directly modeled response (black traces). Note that the match is nearly perfect. For this example MDD not only ensures that the phase and amplitude of the recovered surface waves are correct, it also suppresses the fluctuations in Figure 10d that are caused by the sparse and irregular distribution of noise sources.

6.2 Passive reflected-wave interferometry

Ambient noise is usually dominated by surface waves. Passive reflected-wave interferometry is only possible after careful suppression of surface waves (Draganov et al. 2009).

Figure 11a shows the configuration for passive reflected-wave interferometry by crosscorrelation. The surface $\mathbb{S}_{\mathrm{src}}$ forms together with the Earth's free surface a closed boundary. Sources are only required on the open surface $\mathbb{S}_{\mathrm{src}}$. The correlation function $C(\mathbf{x}_B, \mathbf{x}_A, t)$ involves the crosscorrelation of the full wave fields at $\mathbf{x}_A$ and $\mathbf{x}_B$ (Figure 11a only shows the direct path of $u(\mathbf{x}_A, \mathbf{x}_S, t)$ and the first reflected path of $u(\mathbf{x}_B, \mathbf{x}_S, t)$). The crosscorrelation is integrated over the source positions in case of transient sources (equation 11) or ~~integrated~~ averaged over time in case of uncorrelated noise sources (equation 17). Equation (13) gives the relation between the correlation function $C(\mathbf{x}_B, \mathbf{x}_A, t)$ and the Green's function $G(\mathbf{x}_B, \mathbf{x}_A, t)$, which for the current configuration should be interpreted as the reflection response of the subsurface. It includes primary and multiple reflections (internal multiples and surface-related multiples) as well as a direct wave. Equations (11), (13) and (17) have been derived for the situation that the receivers $\mathbf{x}_A$ and $\mathbf{x}_B$ are in $\mathbb{V}$. In that case u stands for acoustic pressure (p) and $G(\mathbf{x}_B, \mathbf{x}_A, t)$ represents the acoustic pressure at $\mathbf{x}_B$ due to an impulsive point source of volume injection rate at source position $\mathbf{x}_A$. The equations remain valid when the receivers $\mathbf{x}_A$ and $\mathbf{x}_B$ are at the free surface. In that case u stands for the normal particle velocity (v) and $G(\mathbf{x}_B, \mathbf{x}_A, t)$ represents the normal particle velocity at $\mathbf{x}_B$ due to an impulsive normal traction source at $\mathbf{x}_A$ (Wapenaar & Fokkema 2006).

We illustrate this method with a numerical example. Consider the configuration in Figure 12a, which consists of a horizontally layered target below a homogeneous overburden. The green triangles at the free surface denote 51 regularly spaced vertical geophones with spacing $\Delta x_1 = 40\mathrm{m}$ (only nine geophones are shown). The blue dots below the layered target denote 250 irregularly spaced uncorrelated noise sources with an average lateral spacing of $\Delta x_1 = 20\mathrm{m}$ and a central frequency of 22 Hz. Note the clustering of sources around $x_1 \approx -1400\mathrm{m}$ and $x_1 \approx 500\mathrm{m}$. The responses of these sources are shown in Figure 12b (only 3 s of 25 minutes of noise is shown). We denote these responses as $v(\mathbf{x}_A, t)$ and $v(\mathbf{x}_B, t)$, where $\mathbf{x}_A$ and $\mathbf{x}_B$ can be any of the
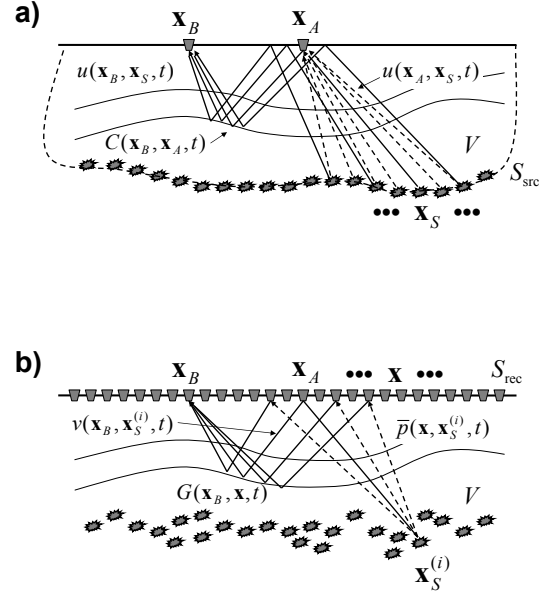

Figure 11. *Configurations for passive reflected-wave interferometry. (a) In the crosscorrelation method the full wavefields $u(\mathbf{x}_A, \mathbf{x}_S, t)$ and $u(\mathbf{x}_B, \mathbf{x}_S, t)$ are correlated and integrated along the sources on $\mathbb{S}_{\mathrm{src}}$. The correlation function $C(\mathbf{x}_B, \mathbf{x}_A, t)$ is proportional to $G(\mathbf{x}_B, \mathbf{x}_A, t) + G(\mathbf{x}_B, \mathbf{x}_A, -t)$, convolved with the autocorrelation of the sources. (b) The convolutional model used for interferometry by MDD. The response $v(\mathbf{x}_B, \mathbf{x}_S^{(i)}, t) - \bar{v}(\mathbf{x}_B, \mathbf{x}_S^{(i)}, t)$ is equal to the convolution of the Green's function $G(\mathbf{x}_B, \mathbf{x}, t)$ and the reference wave field $\bar{p}(\mathbf{x}, \mathbf{x}_S^{(i)}, t)$, integrated along the receivers at $\mathbb{S}_{\mathrm{rec}}$.*

51 geophones. We evaluate the correlation function

$$C_{v,v}(\mathbf{x}_B, \mathbf{x}_A, t) = \langle v(\mathbf{x}_B, t) * v(\mathbf{x}_A, -t) \rangle, \qquad (60)$$

averaged over 25 minutes of noise. The result is shown in Figure 12c for fixed $\mathbf{x}_A$ (geophone number 26) and variable $\mathbf{x}_B$ (geophones $1 - 51$). According to equation (13) this correlation function ~~equals~~ is proportional to ~~$(\rho c/2)$~~ $\{G(\mathbf{x}_B, \mathbf{x}_A, t) + G(\mathbf{x}_B, \mathbf{x}_A, -t)\} * S(t)$. Figure 12d shows a zoomed version of the causal part of the correlation function $C_{v,v}(\mathbf{x}_B, \mathbf{x}_A, t)$ (the red traces) and the modeled reflection response $G^{\mathrm{s}}(\mathbf{x}_B, \mathbf{x}_A, t) * S(t)$ with the source $\mathbf{x}_A$ at the position of geophone 26 (the black traces). Here $G^{\mathrm{s}}(\mathbf{x}_B, \mathbf{x}_A, t)$ is the scattered Green's function, i.e., the total Green's function $G(\mathbf{x}_B, \mathbf{x}_A, t)$ minus the direct wave. Note that the arrival times of the correlation function nicely match those of the directly modeled reflection response, but the wave forms and amplitudes are not accurately reconstructed. This discrepancy is a consequence of the irregular source distribution, in particular the clustering around $x_1 \approx -1400\mathrm{m}$ and $x_1 \approx 500\mathrm{m}$ (Figure 12a), which implies that the integral along $\mathbb{S}_{\mathrm{src}}$ (Figure 11a) is not properly discretized.

Next we discuss passive reflected-wave interferometry by MDD. Figure 11b shows the modified configuration. This configuration is different from other MDD configurations discussed in this paper in the sense that the source positions $\mathbf{x}_S^{(i)}$ are now in $\mathbb{V}$. Hence, because this configuration is
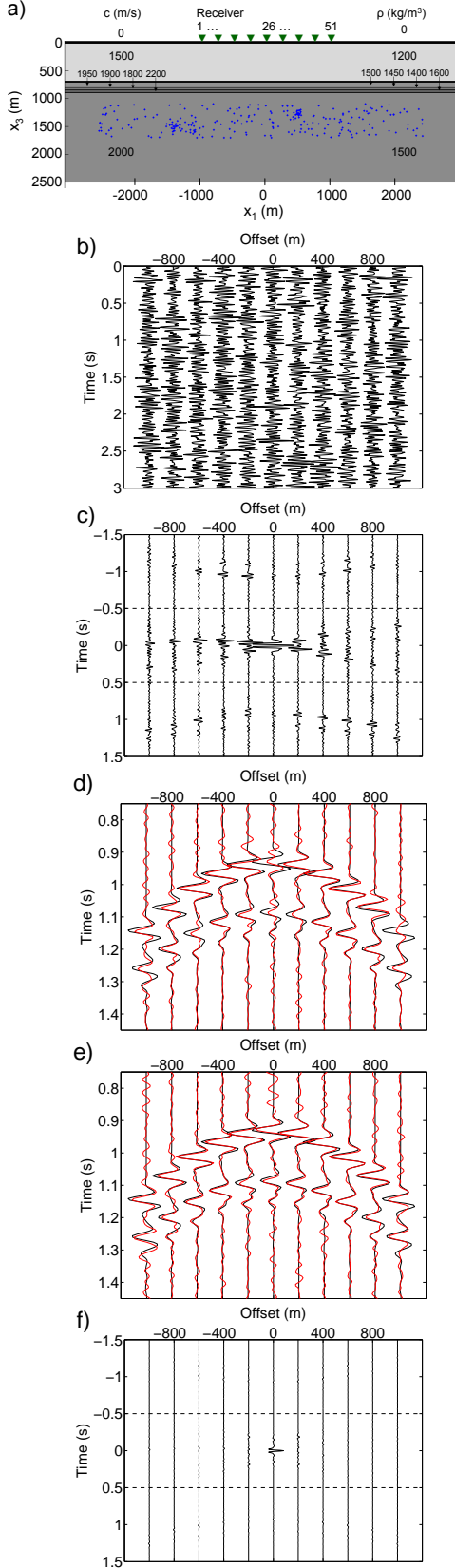
Figure 12. *Numerical example of ambient-noise reflected-wave interferometry. (a) Configuration with a horizontally layered target below a homogeneous overburden and a free surface. There is an irregular distribution of uncorrelated noise sources below the target. (b) Modeled noise response, observed by receivers at the free surface. (c) Correlation function $C_{v,v}(\mathbf{x}_B, \mathbf{x}_A, t) = \langle v(\mathbf{x}_B, t) * v(\mathbf{x}_A, -t) \rangle$ (fixed $\mathbf{x}_A$, variable $\mathbf{x}_B$), clipped at 20 % of the maximum amplitude. (d) Zoomed version of the causal part of the correlation function (red traces), compared with the directly modeled scattered part of the Green's function, $G^{\mathrm{s}}(\mathbf{x}_B, \mathbf{x}_A, t) * S(t)$. (e) Idem, for the MDD result. This was obtained by deconvolving the causal events in (c) by the point-spread function (the strong event in (c) around $t = 0$). (f) Directly modeled correlation function $C_{v^{\mathrm{s}}, v^{\mathrm{s}}}(\mathbf{x}_B, \mathbf{x}_A, t)$ (same amplitude scaling as in c). This weak event is ignored in the MDD method.*

not a special case of that in Figure 1b we cannot make use of equation (27) without making some modifications. We previously dealt with the configuration of Figure 11b (Wapenaar et al. 2008b) and derived the following convolution-type representation

$$v(\mathbf{x}_B, \mathbf{x}_S^{(i)}, t) - \bar{v}(\mathbf{x}_B, \mathbf{x}_S^{(i)}, t) =$$
$$\int_{\mathbb{S}_{\mathrm{rec}}} G(\mathbf{x}_B, \mathbf{x}, t) * \bar{p}(\mathbf{x}, \mathbf{x}_S^{(i)}, t) \, d\mathbf{x}. \quad (61)$$

Here the bars denote a reference situation with absorbing boundary conditions at $\mathbb{S}_{\mathrm{rec}}$. Hence, $\bar{p}(\mathbf{x}, \mathbf{x}_S^{(i)}, t)$ and $\bar{v}(\mathbf{x}_B, \mathbf{x}_S^{(i)}, t)$ are the pressure and normal particle velocity that would be measured at $\mathbb{S}_{\mathrm{rec}}$ in absence of the free surface. The Green's function $G(\mathbf{x}_B, \mathbf{x}, t)$ in equation (61) represents again the normal particle velocity at $\mathbf{x}_B$ due to an impulsive normal traction source at source position $\mathbf{x}$, both at $\mathbb{S}_{\mathrm{rec}}$. It is defined in the actual medium with the free-surface boundary condition at $\mathbb{S}_{\mathrm{rec}}$. For later convenience we subtract the direct wave contribution from both sides of equation (61), yielding

$$v^{\mathrm{s}}(\mathbf{x}_B, \mathbf{x}_S^{(i)}, t) = \int_{\mathbb{S}_{\mathrm{rec}}} G^{\mathrm{s}}(\mathbf{x}_B, \mathbf{x}, t) * \bar{p}(\mathbf{x}, \mathbf{x}_S^{(i)}, t) \, d\mathbf{x}, \quad (62)$$

where $G^{\mathrm{s}}(\mathbf{x}_B, \mathbf{x}, t)$ is again the scattered Green's function (i.e., the total Green's function minus the direct wave) and where

$$v^{\mathrm{s}}(\mathbf{x}_B, \mathbf{x}_S^{(i)}, t) = v(\mathbf{x}_B, \mathbf{x}_S^{(i)}, t) - 2\bar{v}(\mathbf{x}_B, \mathbf{x}_S^{(i)}, t). \quad (63)$$

The factor 2 reflects the fact that the direct wave in $v(\mathbf{x}_B, \mathbf{x}_S^{(i)}, t)$ is twice the direct wave $\bar{v}(\mathbf{x}_B, \mathbf{x}_S^{(i)}, t)$ in the situation without free surface. Note that, despite the differences with equation (27), the form of equation (62) is the same as that of equation (27). Hence, analogous to equation (28) we may write

$$C_{v^{\mathrm{s}}, \bar{p}}(\mathbf{x}_B, \mathbf{x}_A, t) = \int_{\mathbb{S}_{\mathrm{rec}}} G^{\mathrm{s}}(\mathbf{x}_B, \mathbf{x}, t) * \Gamma(\mathbf{x}, \mathbf{x}_A, t) \, d\mathbf{x}, \quad (64)$$

where the correlation function and the point-spread function are defined as

$$C_{v^{\mathrm{s}}, \bar{p}}(\mathbf{x}_B, \mathbf{x}_A, t) = \sum_i v^{\mathrm{s}}(\mathbf{x}_B, \mathbf{x}_S^{(i)}, t) * \bar{p}(\mathbf{x}_A, \mathbf{x}_S^{(i)}, -t), \quad (65)$$

$$\Gamma(\mathbf{x}, \mathbf{x}_A, t) = \sum_i \bar{p}(\mathbf{x}, \mathbf{x}_S^{(i)}, t) * \bar{p}(\mathbf{x}_A, \mathbf{x}_S^{(i)}, -t) \quad (66)$$

in the case of transient sources, or as

$$C_{v^{\mathrm{s}}, \bar{p}}(\mathbf{x}_B, \mathbf{x}_A, t) = \langle v^{\mathrm{s}}(\mathbf{x}_B, t) * \bar{p}(\mathbf{x}_A, -t) \rangle, \quad (67)$$
$$\Gamma(\mathbf{x}, \mathbf{x}_A, t) = \langle \bar{p}(\mathbf{x}, t) * \bar{p}(\mathbf{x}_A, -t) \rangle \quad (68)$$

in the case of uncorrelated noise sources. A complication is that these correlation functions contain fields in a reference situation with an absorbing boundary at $\mathbb{S}_{\mathrm{rec}}$. To see how this can be dealt with for transient sources and for noise sources, consider again the configuration of Figure 12a. When the sources are transients, the first arrivals (including internal multiple scattering in the target) in $v(\mathbf{x}_A, \mathbf{x}_S^{(i)}, t)$ are well separated in time from the surface-related multiples, so the reference response $\bar{v}(\mathbf{x}_A, \mathbf{x}_S^{(i)}, t)$ can be extracted by applying a time window to $v(\mathbf{x}_A, \mathbf{x}_S^{(i)}, t)$ and multiplying the result by one-half. Both $\bar{v}$ and $\bar{p}$ are ~~upgoing~~ outward propagating waves at the absorbing boundary $\mathbb{S}_{\mathrm{rec}}$, so $\bar{p}$ can be

obtained from $\bar{v}$ using the equation of motion and the one-way wave equation for ~~upgoing~~ outward propagating waves, according to

$$-j\omega\rho\hat{\bar{v}} = n_i\partial_i\hat{\bar{p}} = -j\hat{\mathcal{H}}_1\hat{\bar{p}}. \tag{69}$$

~~For example, when the medium directly below $\mathbb{S}_{\text{rec}}$ is homogeneous, we can use the relation~~
~~$\hat{\bar{\tilde{p}}}(\mathbf{p}_A, \mathbf{x}_S^{(i)}, \omega) = (\rho_1/q_A)\hat{\bar{\tilde{v}}}(\mathbf{p}_A, \mathbf{x}_S^{(i)}, \omega),$~~
~~where the tilde denotes the rayparameter frequency $(\mathbf{p}_A, \omega)$ domain, $q_A = \sqrt{1/c_1^2 - \mathbf{p}_A \cdot \mathbf{p}_A}$ is the vertical slowness, and ρ_1 and c_1 are the mass density and propagation velocity, respectively, directly below $\mathbb{S}_{\overline{\text{rec}}}$.~~ Because of the near-vertical incidence of the waves at $\mathbb{S}_{\text{rec}}$, in practice it suffices to make the following approximation

$$\bar{p}(\mathbf{x}_A, \mathbf{x}_S^{(i)}, t) \approx \rho_1 c_1 \bar{v}(\mathbf{x}_A, \mathbf{x}_S^{(i)}, t), \tag{70}$$

where ρ_1 and c_1 are the mass density and propagation velocity, respectively, directly below $\mathbb{S}_{\text{rec}}$. This gives all fields needed in equations (63), (65) and (66) to evaluate the correlation function and the point-spread function, after which $G^{\text{s}}(\mathbf{x}_B, \mathbf{x}, t)$ can be resolved by MDD from equation (64), see Wapenaar et al. (2008b) for a numerical example.

When the sources are noise sources we cannot separate the reference fields from the measured fields by time windowing, but van der Neut et al. (2010) propose to make such a separation in the correlation function, as follows. Using $v = 2\bar{v} + v^{\text{s}}$ (equation 63) we write for the correlation function, as defined in equation (60),

$$C_{v,v}(\mathbf{x}_B, \mathbf{x}_A, t) = \{4C_{\bar{v},\bar{v}} + 2C_{v^{\text{s}},\bar{v}} + 2C_{\bar{v},v^{\text{s}}} + C_{v^{\text{s}},v^{\text{s}}}\}(\mathbf{x}_B, \mathbf{x}_A, t), \tag{71}$$

where

$$
\begin{aligned}
C_{\bar{v},\bar{v}}(\mathbf{x}_B, \mathbf{x}_A, t) &= \langle \bar{v}(\mathbf{x}_B, t) * \bar{v}(\mathbf{x}_A, -t)\rangle, &\tag{72}\\
C_{v^{\text{s}},\bar{v}}(\mathbf{x}_B, \mathbf{x}_A, t) &= \langle v^{\text{s}}(\mathbf{x}_B, t) * \bar{v}(\mathbf{x}_A, -t)\rangle, &\tag{73}\\
C_{\bar{v},v^{\text{s}}}(\mathbf{x}_B, \mathbf{x}_A, t) &= \langle \bar{v}(\mathbf{x}_B, t) * v^{\text{s}}(\mathbf{x}_A, -t)\rangle, &\tag{74}\\
C_{v^{\text{s}},v^{\text{s}}}(\mathbf{x}_B, \mathbf{x}_A, t) &= \langle v^{\text{s}}(\mathbf{x}_B, t) * v^{\text{s}}(\mathbf{x}_A, -t)\rangle. &\tag{75}
\end{aligned}
$$

For the configuration of Figure 12a, the total correlation function $C_{v,v}(\mathbf{x}_B, \mathbf{x}_A, t)$ is shown in Figure 12c (for fixed $\mathbf{x}_A$ and variable $\mathbf{x}_B$). Assuming $C_{v^{\text{s}},v^{\text{s}}}(\mathbf{x}_B, \mathbf{x}_A, t)$ is weak, the other three terms can be easily obtained from Figure 12c. The strong event between the two dashed lines is the correlation of the reference response, $4C_{\bar{v},\bar{v}}(\mathbf{x}_B, \mathbf{x}_A, t)$. The causal event (below the lower dashed line) is $2C_{v^{\text{s}},\bar{v}}(\mathbf{x}_B, \mathbf{x}_A, t)$ and the acausal event (above the upper dashed line) is $2C_{\bar{v},v^{\text{s}}}(\mathbf{x}_B, \mathbf{x}_A, t)$. To invert equation (64), we need $C_{v^{\text{s}},\bar{p}}(\mathbf{x}_B, \mathbf{x}_A, t)$ and $\Gamma(\mathbf{x}, \mathbf{x}_A, t)$, defined in equations (67) and (68), respectively. These can be obtained from $C_{v^{\text{s}},\bar{v}}(\mathbf{x}_B, \mathbf{x}_A, t)$ and $C_{\bar{v},\bar{v}}(\mathbf{x}, \mathbf{x}_A, t)$, respectively. ~~For example, when the medium directly below $\mathbb{S}_{\text{rec}}$ is homogeneous, these functions can be obtained via the rayparameter-frequency domain, according to~~
~~$\tilde{C}_{v^{\text{s}},\bar{p}}(\mathbf{x}_B, \mathbf{p}_A, \omega) = (\rho_1/q_A)\tilde{C}_{v^{\text{s}},\bar{v}}(\mathbf{x}_B, \mathbf{p}_A, \omega),$~~
~~$\tilde{\tilde{\Gamma}}(\mathbf{p}, \mathbf{p}_A, \omega) = (\rho_1^2/qq_A)\tilde{\tilde{C}}_{\bar{v},\bar{v}}(\mathbf{p}, \mathbf{p}_A, \omega).$~~
~~In practice it suffices to make the following approximations~~ Assuming again near-vertical incidence, we obtain

$$
\begin{aligned}
C_{v^{\text{s}},\bar{p}}(\mathbf{x}_B, \mathbf{x}_A, t) &\approx \rho_1 c_1 C_{v^{\text{s}},\bar{v}}(\mathbf{x}_B, \mathbf{x}_A, t), &\tag{76}\\
\Gamma(\mathbf{x}, \mathbf{x}_A, t) &\approx (\rho_1 c_1)^2 C_{\bar{v},\bar{v}}(\mathbf{x}, \mathbf{x}_A, t). &\tag{77}
\end{aligned}
$$

Having determined these functions, $G^{\text{s}}(\mathbf{x}_B, \mathbf{x}, t)$ can again be resolved by MDD from equation (64). The result (for $\mathbf{x} =$

$\mathbf{x}_A$ fixed at the central geophone and variable $\mathbf{x}_B$) is shown in Figure 12e (red traces), where it is compared with the directly modeled scattered Green's function (black traces). Both results have been convolved with $S(t)$ to facilitate the comparison with the correlation of Figure 12d. The MDD result in Figure 12e matches the directly modeled response significantly better than the correlation in Figure 12d.

Note that we assumed that $C_{v^{\text{s}},v^{\text{s}}}(\mathbf{x}_B, \mathbf{x}_A, t)$ is weak. Figure 12f shows this function obtained from direct modeling and displayed with the same amplitude scaling as $C_{v,v}(\mathbf{x}_B, \mathbf{x}_A, t)$ in Figure 12c. We observe that for this example it is indeed weak. The main contribution is concentrated around $t = 0$, so it has only a small effect on the estimated point-spread function, which is obtained (via equations (72) and (77)) from the event between the dashed lines in Figure 12c. When there are strong reflectors in the subsurface, $C_{v^{\text{s}},v^{\text{s}}}(\mathbf{x}_B, \mathbf{x}_A, t)$ may not be weak and distort the estimation of the point-spread function as well as the correlation function $C_{v^{\text{s}},\bar{p}}(\mathbf{x}_B, \mathbf{x}_A, t)$.

An alternative deconvolution approach for passive reflected-wave interferometry is presented by van Groenestijn & Verschuur (2010). Their method does not use the separation of events in the correlation function, but is adaptive and aims to minimize the energy in the estimated reference wave field $\bar{v}(\mathbf{x}_A, t)$. Since the reflections in the total noise field $v(\mathbf{x}_A, t)$ may interfere constructively as well as destructively with the reference noise field $\bar{v}(\mathbf{x}_A, t)$, there is no physical justification that the energy in $\bar{v}(\mathbf{x}_A, t)$ should be minimized. It remains an open question which of the approaches functions best in case of strongly scattering media.

7 DISCUSSION AND CONCLUSIONS

The methodology of seismic interferometry (or Green's function retrieval) by crosscorrelation has a number of attractive properties as well as several limitations. The main attractiveness of the method is that a deterministic medium response can be obtained from controlled-source or passive noise measurements, without the need to know the medium parameters nor the positions of the sources. The fact that this deterministic response is obtained by a straightforward crosscorrelation of two receiver responses has also contributed to the popularity of the method. The main underlying assumptions are that the medium is lossless and that the wave field is equipartitioned, meaning that the net power-flux is (close to) zero (Malcolm et al. 2004; Sánchez-Sesma et al. 2006). It has been shown by Fan & Snieder (2009) that equipartitioning is a necessary but not a sufficient condition.

For open systems the method works well when the receivers that are used in the correlation process are surrounded by a regular distribution of independent transient or uncorrelated noise sources with equal autocorrelation functions. However, in practical situations the method may suffer from irregularities in the source distribution, asymmetric illumination, intrinsic losses, etc.

Figures 3a and 3b illustrate configurations with an irregular source distribution in a finite region, illuminating the medium from one side only. For these configurations, equation (28) shows that the crosscorrelation function $C(\mathbf{x}_B, \mathbf{x}_A, t)$ is a distorted version of the sought Green's function $\bar{G}_{\text{d}}(\mathbf{x}_B, \mathbf{x}, t)$. The distortion is quantified by the

point-spread function $\Gamma(\mathbf{x}, \mathbf{x}_A, t)$, which blurs the source of the Green's function in the spatial directions and generates ghosts in the temporal direction (van der Neut & Thorbecke 2009). As such, this space-time point-spread function plays a similar role as the spatial point-spread function in optical, acoustic and seismic imaging systems (Born & Wolf 1965; Norton 1992; Schuster & Hu 2000). When the point-spread function of an imaging system is known, the resolution of an image can be improved by deconvolving for the point-spread function (Jansson 1997; Hu et al. 2001). For example, early images of the Hubble Space Telescope were blurred by a flaw in the mirror. These images were sharpened by deconvolving for the point-spread function of the flawed mirror (Boden et al. 1996). In a similar way, the blurred source with ghosts of the Green's function obtained by crosscorrelation can be deblurred and deghosted by deconvolving for the space-time point-spread function, i.e., by inverting equation (28) by MDD. An interesting aspect is that the space-time point-spread function can be obtained directly from measured responses, hence, it does not require knowledge of the complex medium nor of the sources. This means that it automatically accounts for the distorting effects of the irregularity of the sources (including variations in their autocorrelation functions), and of the medium inhomogeneities, including multiple scattering.

The MDD method has, of course, also its limitations. First, in order to retrieve the Green's function $\bar{G}_d(\mathbf{x}_B, \mathbf{x}, t)$ it does not suffice to have two receivers only, at $\mathbf{x}$ and $\mathbf{x}_B$, because $\mathbf{x}$ is assumed to be an element of a regular (or regularized) array of receivers along $\mathbb{S}_{\text{rec}}$, see Figure 3. Second, the expressions for the correlation function (equations 29 and 32) and for the point-spread function (equations 30 and 33) contain the inward propagating field $u^{\text{in}}(\mathbf{x}, t)$ on $\mathbb{S}_{\text{rec}}$ (propagating into $\mathbb{V}$). In order to extract this inward propagating field from the total field, either multi-component receivers or two receiver surfaces close to each other are required. Alternatively, when multiple scattering is weak, one could correlate the total fields and extract the point-spread function by applying a time window around $t = 0$. Third, MDD involves an inversion of an integral equation, which in practice is achieved by matrix inversion. ~~Apart from the higher cost (in comparison with the correlation method),~~ This matrix inversion can be unstable. The well-posedness of this inverse problem depends on the number of available sources, the source aperture, the bandwidth, and, for multi-component data, on the number of independent source components. In practical situations a spectral analysis of the point-spread function helps to assess for which spatial and temporal frequencies the inversion can be carried out in a stable sense (van der Neut et al. 2011). Finally, because of the matrix inversion, the costs of the MDD method are higher than those of the correlation method. For the 2D examples in this paper, the costs of the matrix inversions were moderate, despite the fact that we used direct solvers only. For 3D applications we expect that MDD is still feasible, particularly when use is made of iterative solvers.

Despite the mentioned limitations, for applications in which the data are measured with arrays of receivers, Green's function retrieval by MDD has the potential to obtain virtual sources that are better focused and have less distortions by spurious multiples than those obtained by crosscorrelation.

APPENDIX A: ANALYTICAL EVALUATION OF THE POINT-SPREAD FUNCTION

We evaluate the point-spread function, as defined in equation (30), for the situation of a homogeneous lossless medium (propagation velocity c) and a regular distribution of sources with equal autocorrelation functions $S(t)$ along an open source boundary. We rewrite the sum over the source positions $\mathbf{x}_S^{(i)}$ as an integral along the source boundary $\mathbb{S}_{\text{src}}$, hence

$$\Gamma(\mathbf{x}, \mathbf{x}_A, t) = \int_{\mathbb{S}_{\text{src}}} u^{\text{in}}(\mathbf{x}, \mathbf{x}_S, t) * u^{\text{in}}(\mathbf{x}_A, \mathbf{x}_S, -t) \, d\mathbf{x}_S, \tag{A-1}$$

with $\mathbf{x}$ and $\mathbf{x}_A$ at the receiver boundary $\mathbb{S}_{\text{rec}}$. Note that, unlike in equation (11), the source boundary $\mathbb{S}_{\text{src}}$ is not enclosing the receivers, hence, $\Gamma(\mathbf{x}, \mathbf{x}_A, t)$ does not converge to $(\rho c/2)\{G(\mathbf{x}, \mathbf{x}_A, t) + G(\mathbf{x}, \mathbf{x}_A, -t)\} * S(t)$. For the following analysis we let $\mathbb{S}_{\text{src}}$ and $\mathbb{S}_{\text{rec}}$ be two horizontal boundaries, with $\mathbb{S}_{\text{rec}}$ a distance Δx_3 below $\mathbb{S}_{\text{src}}$. For convenience we consider the 2D situation, so the boundary integral becomes a line integral along $x_{1,S}$. For the chosen configuration the fields under the integral are shift-invariant, i.e., they are only functions of the relative distances $x_1 - x_{1,S}$ and $x_{1,A} - x_{1,S}$, respectively. Similarly, the point-spread function is a function of $x_1 - x_{1,A}$ only. Choosing $x_{1,A} = 0$, equation (A-1) can thus be rewritten as

$$\Gamma(x_1, t) = \int_{-\infty}^{\infty} u^{\text{in}}(x_1 - x_{1,S}, \Delta x_3, t) * u^{\text{in}}(-x_{1,S}, \Delta x_3, -t) \, dx_{1,S}. \tag{A-2}$$

We define the double Fourier transform of a space- and time-dependent function $u(x_1, t)$ as

$$\tilde{u}(k_1, \omega) = \int_{-\infty}^{\infty} \int_{-\infty}^{\infty} \exp\{-j(\omega t - k_1 x_1)\} u(x_1, t) \, dt dx_1. \tag{A-3}$$

Hence, equation (A-2) transforms to

$$\tilde{\Gamma}(k_1, \omega) = \tilde{u}^{\text{in}}(k_1, \Delta x_3, \omega) \{\tilde{u}^{\text{in}}(k_1, \Delta x_3, \omega)\}^*. \tag{A-4}$$

In section 4.2 we argued that the basic representation for MDD (equation (27)) holds irrespective of the type of sources at $\mathbb{S}_{\text{src}}$. For convenience of the analysis we consider dipole sources emitting a signal $s(t)$ (this is for example representative for the situation of vertically oriented vibrators at a free surface). The expression for $\tilde{u}^{\text{in}}(k_1, \Delta x_3, \omega)$ is thus given by

$$\tilde{u}^{\text{in}}(k_1, \Delta x_3, \omega) = \tag{A-5}$$

$$\hat{s}(\omega) \times \begin{cases} \exp\{-j \operatorname{sgn}(\omega) \sqrt{k^2 - k_1^2} \, \Delta x_3\} & \text{for} \quad k_1^2 \leq k^2 \\ \exp\{-\sqrt{k_1^2 - k^2} \, \Delta x_3\} & \text{for} \quad k_1^2 > k^2, \end{cases}$$

with $k = \omega/c$. Substitution into equation (A-4) gives

$$\tilde{\Gamma}(k_1, \omega) = \hat{S}(\omega) \times \begin{cases} 1 & \text{for} \quad k_1^2 \leq k^2 \\ \exp\{-2\sqrt{k_1^2 - k^2}\,\Delta x_3\} & \text{for} \quad k_1^2 > k^2, \end{cases}$$
$$(A-6)$$

with $\hat{S}(\omega) = |\hat{s}(\omega)|^2$. Hence, for propagating waves ($k_1^2 \leq k^2$) the Fourier-transformed point-spread function $\tilde{\Gamma}(k_1, \omega)$ is equal to the power spectrum $\hat{S}(\omega)$ of the dipole sources, whereas for evanescent waves ($k_1^2 > k^2$) it is exponentially decaying. Note that for the limit $\Delta x_3 \to 0$ the point-spread function approaches $\hat{S}(\omega)$ for all k_1. Hence, for this case we have $\lim_{\Delta x_3 \to 0} \Gamma(x_1, t) = \{\delta(x_1)\delta(t)\} * S(t)$, meaning that the only band-limitation is caused by the autocorrelation of the sources. However, for any realistic value of Δx_3 the exponentially decaying character of the evanescent waves imposes a more serious band-limitation to the delta function. Already for Δx_3 larger than a few wavelengths it is reasonable to approximate the exponentially decaying term in equation (A-6) by zero for all $k_1^2 > k^2$, meaning that for a given frequency ω the pass-band is $-|\omega|/c \leq k_1 \leq |\omega|/c$. Hence, the inverse transformation to the space-frequency domain is obtained as

$$\begin{aligned} \hat{\Gamma}(x_1, \omega) &= \frac{1}{2\pi} \int_{-\infty}^{\infty} \tilde{\Gamma}(k_1, \omega) \exp(-jk_1 x_1)\,\mathrm{d}k_1 \\ &= \frac{\hat{S}(\omega)}{2\pi} \int_{-|\omega|/c}^{|\omega|/c} \exp(-jk_1 x_1)\,\mathrm{d}k_1 \\ &= \frac{\sin(|\omega|x_1/c)}{\pi x_1} \hat{S}(\omega). \qquad (A-7) \end{aligned}$$

Note that this expression is identical to the resolution function for 2D seismic migration (Berkhout 1984). When the source array is finite, the pass-band is further reduced to $-|\omega|\sin\alpha_{\max}/c \leq k_1 \leq |\omega|\sin\alpha_{\max}/c$, where $\alpha_{\max}$ is the maximum propagation angle. Hence, for this situation we replace the velocity c in equation (A-7) by the apparent velocity $c_a = c/\sin\alpha_{\max}$. To obtain the space-time domain expression we first rewrite equation (A-7) as

$$\begin{aligned} \hat{\Gamma}(x_1, \omega) &= -j\,\mathrm{sgn}(\omega)\frac{j\sin(\omega x_1/c_a)}{\pi x_1}\hat{S}(\omega) \qquad (A-8) \\ &= -j\,\mathrm{sgn}(\omega)\frac{\exp(j\omega x_1/c_a) - \exp(-j\omega x_1/c_a)}{2\pi x_1}\hat{S}(\omega). \end{aligned}$$

This product of three functions in the frequency domain transforms to a convolution of the corresponding time-domain functions, as follows

$$\Gamma(x_1, t) = \frac{1}{\pi t} * \frac{\delta(t + x_1/c_a) - \delta(t - x_1/c_a)}{2\pi x_1} * S(t). \quad (A-9)$$

For $x_1 \neq 0$ this gives

$$\Gamma(x_1, t) = \frac{1}{2\pi^2 x_1}\left[\frac{1}{t + x_1/c_a} - \frac{1}{t - x_1/c_a}\right] * S(t), \quad (A-10)$$

and for $x_1 \to 0$

$$\Gamma(0, t) = \frac{1}{\pi^2 c_a t} * \frac{\partial S(t)}{\partial t}. \qquad (A-11)$$

$\Gamma(x_1, t)$ is illustrated in Figure A1 for $c = 2000$ m/s, $\alpha_{\max} = \pi/2$ (corresponding to an infinite source array) and $S(t)$ a Ricker wavelet with a central frequency of 20 Hz. Note that $\Gamma(x_1, t)$ reveals an X-pattern with the maximum amplitude at $(x_1, t) = (0, 0)$ and decaying amplitudes along lines $t = \pm x_1/c$. The point-spread function $\Gamma(x_1, t)$ can be seen
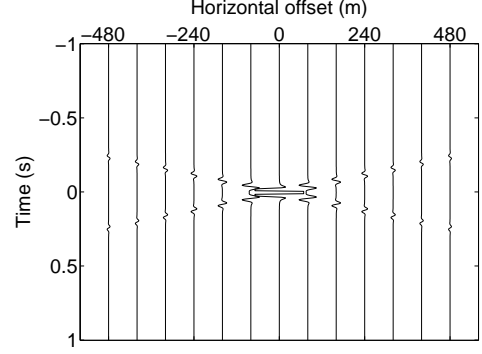

Figure A1. *The space-time point-spread function $\Gamma(x_1, t)$ (clipped at 20% of its maximum amplitude) for the situation of a homogeneous lossless medium (propagation velocity 2000 m/s) and an infinite regular source array. The autocorrelation of the sources is a Ricker wavelet with a central frequency of 20 Hz.*

as a band-limited delta function $\delta(x_1)\delta(t)$, with the temporal band-limit imposed by the autocorrelation function $S(t)$ and the spatial band-limit imposed by the evanescent waves and, for a finite source array, the absence of large propagation angles.

For the derivation in this appendix we considered a 2D configuration and assumed the sources are dipoles. For other situations (3D configuration and/or monopole sources) the details are different, but in all cases the analytical point-spread function reveals the characteristic X-pattern (or a two-sided conical pattern in 3D).

REFERENCES

Amundsen, L., 2001. Elimination of free-surface related multiples without need of the source wavelet, *Geophysics*, **66**(1), 327–341.

Amundsen, L. & Reitan, A., 1995. Decomposition of multicomponent sea-floor data into upgoing and downgoing P- and S-waves, *Geophysics*, **60**, 563–572.

Amundsen, L., Løseth, L., Mittet, R., Ellingsrud, S., & Ursin, B., 2006. Decomposition of electromagnetic fields into upgoing and downgoing components, *Geophysics*, **71**(5), G211–G223.

Bagaini, C., 2006. Overview of simultaneous Vibroseis acquisition methods, in SEG, Expanded Abstracts, pp. 70–74.

Bakulin, A. & Calvert, R., 2004. Virtual source: new method for imaging and 4D below complex overburden, in SEG, Expanded Abstracts, pp. 2477–2480.

Bakulin, A. & Calvert, R., 2006. The virtual source method: Theory and case study, *Geophysics*, **71**(4), SI139–SI150.

Beasley, C. J., Chambers, R. E., & Jiang, Z., 1998. A new look at simultaneous sources, in SEG, Expanded Abstracts, pp. 133–135.

Bensen, G. D., Ritzwoller, M. H., Barmin, M. P., Levshin, A. L., Lin, F., Moschetti, M. P., Shapiro, N. M., & Yang, Y., 2007. Processing seismic ambient noise data to obtain reliable broadband surface wave dispersion measurements, *Geophysical Journal International*, **169**, 1239–1260.

Bensen, G. D., Ritzwoller, M. H., & Shapiro, N. M., 2008. Broadband ambient noise surface wave tomography across the United States, *Journal of Geophysical Research - Solid Earth*, **113**, B05306–1–B05306–21.

Berkhout, A. J., 1982. *Seismic Migration. Imaging of acoustic energy by wave field extrapolation*, Elsevier.

Berkhout, A. J., 1984. *Seismic resolution. A quantitative analysis of resolving power of acoustical echo techniques*, Geophysical Press, London.

Berkhout, A. J., 2008. Changing the mindset in seismic data acquisition, *The Leading Edge*, **27**(7), 924–938.

Boden, A. F., Redding, D. C., Hanisch, R. J., & Mo, J., 1996. Massively parallel spatially variant maximum-likelihood restoration of Hubble Space Telescope imagery, *Journal of the Optical Society of America. A: Optics, image science and vision*, **13**, 1537–1545.

Born, M. & Wolf, E., 1965. *Principles of optics*, Pergamon Press, London.

Bromirski, P. D., 2001. Vibrations from the "Perfect Storm", *Geochemistry Geophysics Geosystems*, **2**, 1030.

Campillo, M. & Paul, A., 2003. Long-range correlations in the diffuse seismic coda, *Science*, **299**, 547–549.

Curtis, A. & Halliday, D., 2010. Directional balancing for seismic and general wavefield interferometry, *Geophysics*, **75**(1), SA1–SA14.

Draganov, D., Campman, X., Thorbecke, J., Verdel, A., & Wapenaar, K., 2009. Reflection images from ambient seismic noise, *Geophysics*, **74**(5), A63–A67.

Duijndam, A. J. W., Schonewille, M. A., & Hindriks, C. O. H., 1999. Reconstruction of band-limited signals, irregularly sampled along one spatial direction, *Geophysics*, **64**, 524–538.

Dziewonski, A. M. & Anderson, D. L., 1981. Preliminary reference Earth model, *Physics of the Earth and Planetary Interiors*, **25**, 297–356.

Ellingsrud, S., Eidesmo, T., Johansen, S., Sinha, M. C., MacGregor, L. M., & Constable, S., 2002. Remote sensing of hydrocarbon layers by seabed logging (SBL): Results from a cruise offshore Angola, *The Leading Edge*, **21**(10), 972–982.

Esmersoy, C. & Oristaglio, M., 1988. Reverse-time wave-field extrapolation, imaging, and inversion, *Geophysics*, **53**, 920–931.

Fan, Y. & Snieder, R., 2009. Required source distribution for interferometry of waves and diffusive fields, *Geophysical Journal International*, **179**, 1232–1244.

Fan, Y., Snieder, R., & Singer, J., 2009. 3-D controlled source electromagnetic (CSEM) interferometry by multi-dimensional deconvolution, in SEG, Expanded Abstracts, pp. 779–784.

Fishman, L., 1993. One-way propagation methods in direct and inverse scalar wave propagation modeling, *Radio Science*, **28**(5), 865–876.

Fishman, L. & McCoy, J. J., 1984. Derivation and application of extended parabolic wave theories. I. The factorized Helmholtz equation, *J. Math. Phys.*, **25**(2), 285–296.

Frijlink, M. & Wapenaar, K., 2010. Reciprocity theorems for one-way wave fields in curvilinear coordinate systems, *SIAM Journal on Imaging Sciences*, **3**(3), 390–415.

Gabriels, P., Snieder, R., & Nolet, G., 1987. In situ measurements of shear-wave velocity in sediments with higher-mode Rayleigh waves, *Geophysical Prospecting*, **35**, 187–196.

Gelius, L.-J., Lecomte, I., & Tabti, H., 2002. Analysis of the resolution function in seismic prestack depth imaging, *Geophysical Prospecting*, **50**, 505–515.

Gerstoft, P., Sabra, K. G., Roux, P., Kuperman, W. A., & Fehler, M. C., 2006. Green's functions extraction and surface-wave tomography from microseisms in southern California, *Geophysics*, **71**(4), SI23–SI31.

Gouédard, P., Roux, P., Campillo, M., & Verdel, A., 2008a. Convergence of the two-point correlation function toward the Green's function in the context of a seismic-prospecting data set, *Geophysics*, **73**(6), V47–V53.

Gouédard, P., Stehly, L., Brenguier, F., Campillo, M., Colin de Verdière, Y., Larose, E., Margerin, L., Roux, P., Sánchez-Sesma, F. J., Shapiro, N. M., & Weaver, R. L., 2008b. Cross-correlation of random fields: mathematical approach and applications, *Geophysical Prospecting*, **56**, 375–393.

Halliday, D. & Curtis, A., 2008. Seismic interferometry, surface waves and source distribution, *Geophysical Journal International*, **175**, 1067–1087.

Halliday, D. & Curtis, A., 2010. An interferometric theory of source-receiver scattering and imaging, *Geophysics*, **75**(6), SA95–SA103.

Hampson, G., Stefani, J., & Herkenhoff, F., 2008. Acquisition using simultaneous sources, *The Leading Edge*, **27**(7), 918–923.

Howe, D., Foster, M., Allen, T., Taylor, B., & Jack, I., 2007. Independent simultaneous sweeping A method to increase the productivity of land seismic crews, in SEG, Expanded Abstracts, pp. 2826–2830.

Hu, J., Schuster, G. T., & Valasek, P., 2001. Poststack migration deconvolution, *Geophysics*, **66**, 939–952.

Hunziker, J., van der Neut, J., Slob, E., & Wapenaar, K., 2009. Controlled source interferometry with noisy data, in SEG, Expanded Abstracts, pp. 689–693.

Hunziker, J., Fan, Y., Slob, E., Snieder, R., & Wapenaar, K., 2011. Two-dimensional controlled-source electromagnetic interferometry by multidimensional deconvolution: spatial sampling aspects, *Geophysical Prospecting*, **xx**, xx–xx.

Ikelle, L., 2007. Coding and decoding: seismic data modeling, acquisition and processing, in SEG, Expanded Abstracts, pp. 66–70.

Jansson, P., 1997. *Deconvolution of images and spectra*, Academic Press.

Kimman, W. P. & Trampert, J., 2010. Approximations in seismic interferometry and their effects on surface waves, *Geophysical Journal International*, **182**, 461–476.

Korneev, V. & Bakulin, A., 2006. On the fundamentals of the virtual source method, *Geophysics*, **71**(3), A13–A17.

Larose, E., Margerin, L., Derode, A., van Tiggelen, B., Campillo, M., Shapiro, N., Paul, A., Stehly, L., & Tanter, M., 2006. Correlation of random wave fields: An interdisciplinary review, *Geophysics*, **71**(4), SI11–SI21.

Lecomte, I., 2008. Resolution and illumination analyses in PSDM: A ray-based approach, *The Leading Edge*, **27**(5), 650–663.

Liang, C. & Langston, C. A., 2008. Ambient seismic noise tomography and structure of eastern North America, *Journal of Geophysical Research - Solid Earth*, **113**, B03309–1–B03309–18.

Lin, F.-C., Ritzwoller, M. H., & Snieder, R., 2009. Eikonal tomography: surface wave tomography by phase front tracking across a regional broad-band seismic array, *Geophysical Journal International*, **177**, 1091–1110.

Ma, S., Prieto, G. A., & Beroza, G. C., 2008. Testing community velocity models for Southern California using the ambient seismic field, *Bulletin of the Seismological Society of America*, **98**, 2694–2714.

Malcolm, A. E., Scales, J. A., & van Tiggelen, B. A., 2004. Extracting the Green function from diffuse, equipartitioned waves, *Physical Review E*, **70**, 015601(R)–1–015601(R)–4.

Mehta, K., Bakulin, A., Sheiman, J., Calvert, R., & Snieder, R., 2007a. Improving the virtual source method by wavefield separation, *Geophysics*, **72**(4), V79–V86.

Mehta, K., Snieder, R., & Graizer, V., 2007b. Extraction of near-surface properties for a lossy layered medium using the propagator matrix, *Geophysical Journal International*, **169**, 271–280.

Menke, W., 1989. *Geophysical data analysis*, Academic Press.

Miller, D., Oristaglio, M., & Beylkin, G., 1987. A new slant on seismic imaging: Migration and integral geometry, *Geophysics*, **52**, 943–964.

Minato, S., Matsuoka, T., Tsuji, T., Draganov, D., Hunziker, J., & Wapenaar, K., 2011. Seismic interferometry using multidimensional deconvolution and crosscorrelation for crosswell seismic reflection data without borehole sources, *Geophysics*, **76**(1), in press.

Miyazawa, M., Snieder, R., & Venkataraman, A., 2008. Application of seismic interferometry to extract P- and S-wave propagation and observation of shear-wave splitting from noise data at Cold Lake, Alberta, Canada, *Geophysics*, **73**(4), D35–D40.

Moser, J., Poupon, M., Meyer, H.-J., Wojcik, C., Rosenquist, M., Adejonwo, A., & Smit, D., 2006. Integration of electromagnetic and seismic data to assess residual gas risk in the toe-thrust belt of deepwater Niger Delta, *The Leading Edge*, **25**(8), 977–982.

Muijs, R., Robertsson, J. O. A., & Holliger, K., 2007. Prestack depth migration of primary and surface-related multiple reflections: Part i imaging, *Geophysics*, **72**(2), S59–S69.

Nolet, G., 1975. Higher Rayleigh modes in Western Europe, *Geophysical Research Letters*, **2**, 60–62.

Norton, S. J., 1992. Annular array imaging with full-aperture resolution, *Journal of the Acoustical Society of America*, **92**, 3202–3206.

Oristaglio, M. L., 1989. An inverse scattering formula that uses all the data, *Inverse Problems*, **5**, 1097–1105.

Picozzi, M., Parolai, S., Bindi, D., & Strollo, A., 2009. Characterization of shallow geology by high-frequency seismic noise tomography, *Geophysical Journal International*, **176**, 164–174.

Porter, R. P., 1970. Diffraction-limited, scalar image formation with holograms of arbitrary shape, *Journal of the Optical Society of America*, **60**, 1051–1059.

Riley, D. C. & Claerbout, J. F., 1976. 2-D multiple reflections, *Geophysics*, **41**, 592–620.

Ruigrok, E., Campman, X., Draganov, D., & Wapenaar, K., 2010. High-resolution lithospheric imaging with seismic interferometry, *Geophysical Journal International*, **183**, 339–357.

Sabra, K. G., Gerstoft, P., Roux, P., Kuperman, W. A., & Fehler, M. C., 2005a. Surface wave tomography from microseisms in Southern California, *Geophysical Research Letters*, **32**, L14311–1–L14311–4.

Sabra, K. G., Gerstoft, P., Roux, P., Kuperman, W. A., & Fehler, M. C., 2005b. Extracting time-domain Green's function estimates from ambient seismic noise, *Geophysical Research Letters*, **32**, L03310–1–L03310–5.

Sánchez-Sesma, F. J., Pérez-Ruiz, J. A., Campillo, M., & Luzón, F., 2006. Elastodynamic 2D Green function retrieval from cross-correlation: Canonical inclusion problem, *Geophysical Research Letters*, **33**, L13305–1–L13305–6.

Schalkwijk, K. M., Wapenaar, C. P. A., & Verschuur, D. J., 2003. Adaptive decomposition of multicomponent ocean-bottom seismic data into downgoing and upgoing P- and S-waves, *Geophysics*, **68**, 1091–1102.

Schuster, G. T., 2009. *Seismic interferometry*, Cambridge University Press.

Schuster, G. T. & Hu, J., 2000. Green's function for migration: Continuous recording geometry, *Geophysics*, **65**, 167–175.

Schuster, G. T. & Zhou, M., 2006. A theoretical overview of model-based and correlation-based redatuming methods, *Geophysics*, **71**(4), SI103–SI110.

Shapiro, N. M. & Campillo, M., 2004. Emergence of broadband Rayleigh waves from correlations of the ambient seismic noise, *Geophysical Research Letters*, **31**, L07614–1–L07614–4.

Shapiro, N. M., Campillo, M., Stehly, L., & Ritzwoller, M. H., 2005. High-resolution surface-wave tomography from ambient seismic noise, *Science*, **307**, 1615–1618.

Slob, E. & Wapenaar, K., 2007. GPR without a source: Cross-correlation and cross-convolution methods, *IEEE Transactions on Geoscience and Remote Sensing*, **45**, 2501–2510.

Slob, E., Wapenaar, K., & Snieder, R., 2007. Interferometry in dissipative media: Addressing the shallow sea problem for Seabed Logging applications, in SEG, Expanded Abstracts, pp. 559–563.

Snieder, R., Sheiman, J., & Calvert, R., 2006a. Equivalence of the virtual-source method and wave-field deconvolution in seismic interferometry, *Physical Review E*, **73**, 066620–1–066620–9.

Snieder, R., Wapenaar, K., & Larner, K., 2006b. Spurious multiples in seismic interferometry of primaries, *Geophysics*, **71**(4), SI111–SI124.

Snieder, R., Miyazawa, M., Slob, E., Vasconcelos, I., & Wapenaar, K., 2009. A comparison of strategies for seismic interferometry, *Surveys in Geophysics*, **30**, 503–523.

Stefani, J., Hampson, G., & Herkenhoff, E. F., 2007. Acquisition using simultaneous sources, in EAGE, Extended Abstracts, p. Session: B006.

Tanter, M., Thomas, J.-L., & Fink, M., 2000. Time-reversal and the inverse filter, *Journal of the Acoustical Society of America*, **108**(1), 223–234.

Thorbecke, J. & Wapenaar, K., 2007. On the relation between seismic interferometry and the migration resolution function, *Geophysics*, **72**(6), T61–T66.

Toxopeus, G., Thorbecke, J., Wapenaar, K., Petersen, S., Slob, E., & Fokkema, J., 2008. Simulating migrated and inverted seismic data by filtering a geologic model, *Geophysics*, **73**(2), T1–T10.

Ursin, B., 1983. Review of elastic and electromagnetic wave propagation in horizontally layered media, *Geophysics*, **48**, 1063–1081.

van den Berg, P. M., Abubakar, A., & Habashy, T. M., 2008. Removal of sea-surface-related wavefields and source replacement in CSEM data processing, in SEG, Expanded Abstracts, pp. 672–676.

van der Neut, J. & Bakulin, A., 2009. Estimating and correcting the amplitude radiation pattern of a virtual source, *Geophysics*, **74**(2), SI27–SI36.

van der Neut, J. & Thorbecke, J., 2009. Resolution function for controlled-source seismic interferometry: a data-driven diagnosis, in SEG, Expanded Abstracts, pp. 4090–4094.

van der Neut, J. & Wapenaar, K., 2009. Controlled-source elastodynamic interferometry by cross-correlation of decomposed wavefields, in EAGE, Extended Abstracts, p. Session: X044.

van der Neut, J., Ruigrok, E., Draganov, D., & Wapenaar, K., 2010. Retrieving the earth's reflection response by multidimensional deconvolution of ambient seismic noise, in EAGE, Extended Abstracts, p. Session: P406.

van der Neut, J., Thorbecke, J., Mehta, K., Slob, E., & Wapenaar, K., 2011. Controlled-source interferometric redatuming by cross-correlation and multi-dimensional deconvolution in elastic media, *Geophysics*, **76**, (submitted).

van Groenestijn, G. J. A. & Verschuur, D. J., 2010. Estimation of primaries by sparse inversion from passive seismic data, *Geophysics*, **75**(4), SA61–SA69.

van Manen, D.-J., Robertsson, J. O. A., & Curtis, A., 2005. Modeling of wave propagation in inhomogeneous media, *Physical Review Letters*, **94**, 164301–1–164301–4.

van Veldhuizen, E. J., Blacquière, G., & Berkhout, A. J., 2008. Acquisition geometry analysis in complex 3D media, *Geophysics*, **73**(5), Q43–Q58.

Vasconcelos, I. & Snieder, R., 2008a. Interferometry by deconvolution: Part 1 - Theory for acoustic waves and numerical examples, *Geophysics*, **73**(3), S115–S128.

Vasconcelos, I. & Snieder, R., 2008b. Interferometry by deconvolution: Part 2 - Theory for elastic waves and application to drill-bit seismic imaging, *Geophysics*, **73**(3), S129–S141.

Vasconcelos, I., Snieder, R., & Hornby, B., 2008. Imaging internal multiples from subsalt VSP data - Examples of target-oriented interferometry, *Geophysics*, **73**(4), S157–S168.

Wapenaar, C. P. A. & Berkhout, A. J., 1989. *Elastic wave field extrapolation*, Elsevier, Amsterdam.

Wapenaar, C. P. A., Dillen, M. W. P., & Fokkema, J. T., 2001. Reciprocity theorems for electromagnetic or acoustic one-way wave fields in dissipative inhomogeneous media, *Radio Science*, **36**, 851–863.

Wapenaar, K. & Fokkema, J., 2006. Green's function representations for seismic interferometry, *Geophysics*, **71**(4), SI33–SI46.

Wapenaar, K., Fokkema, J., Dillen, M., & Scherpenhuijsen, P., 2000. One-way acoustic reciprocity and its applications in multiple elimination and time-lapse seismics, in SEG, Expanded Abstracts, pp. 2377–2380.

Wapenaar, K., Fokkema, J., & Snieder, R., 2005. Retrieving the Green's function in an open system by cross-correlation: a comparison of approaches (L), *Journal of the Acoustical Society of America*, **118**, 2783–2786.

Wapenaar, K., Slob, E., & Snieder, R., 2008a. Seismic and electromagnetic controlled-source interferometry in dissipative media, *Geophysical Prospecting*, **56**, 419–434.

Wapenaar, K., van der Neut, J., & Ruigrok, E., 2008b. Passive seismic interferometry by multi-dimensional deconvolution, *Geophysics*, **73**(6), A51–A56.

Wathelet, M. D., Jongmans, D., & Ohrnberger, M., 2004. Surface-wave inversion using a direct search algorithm and its application to ambient vibration measurements, *Near Surface Geophysics*, **2**, 211–221.

Yao, H., van der Hilst, R. D., & de Hoop, M. V., 2006. Surface-wave array tomography in SE Tibet from ambient seismic noise and two-station analysis - I. Phase velocity maps, *Geophysical Journal International*, **166**, 732–744.

Yao, H., Beghein, C., & van der Hilst, R. D., 2008. Surface-wave array tomography in SE Tibet from ambient seismic noise and two-station analysis - II. Crustal and upper-mantle structure, *Geophysical Journal International*, **173**, 205–219.

Yu, J., Hu, J., Schuster, G. T., & Estill, R., 2006. Prestack migration deconvolution, *Geophysics*, **71**(2), S53–S62.

Zheng, Y., 2010. Retrieving the exact Green's function by wavefield crosscorrelation, *Journal of the Acoustical Society of America*, **127**(3), EL93–EL98.

Zheng, Y., He, Y., & Fehler, M. C., 2011. Crosscorrelation kernels in acoustic Green's function retrieval by wavefield correlation for point sources on a plane and a sphere, *Geophysical Journal International*, **xxx**, (in press).